Shake-Table Testing of a Full-Scale 10-Story Resilient Mass Timber Building

Shiling Pei, F.ASCE[1]; Keri L. Ryan, A.M.ASCE[2]; Jeffrey W. Berman, A.M.ASCE[3]; John W. van de Lindt, F.ASCE[4]; Steve Pryor, M.ASCE[5]; Da Huang[6]; Sarah Wichman, A.M.ASCE[7]; Aleesha Busch[8]; William Roser, A.M.ASCE[9]; Sir Lathan Wynn[10]; Yi-en Ji[11]; Tara Hutchinson, M.ASCE[12]; Shokrullah Sorosh, S.M.ASCE[13]; Reid B. Zimmerman, M.ASCE[14]; and James Dolan, F.ASCE[15]

Abstract: As part of a collaborative research effort (The NHERI TallWood Project), an extensive shake table test program was undertaken on a full-scale 10-story mass timber building with a resilient posttensioned mass timber rocking wall lateral system. Over a three-year period, academic and industry partners collaborated on the design, construction, and testing of a 34 m (113 ft) tall, 10-story mass timber building at the world's largest outdoor shake table facility (NHERI@UC San Diego). The test building incorporated a resilient mass timber rocking wall lateral system, gravity connection details designed to remain damage-free under design level earthquakes as well as innovative nonstructural systems detailed to tolerate moderate building drifts without significant damage. A total of 88 earthquake tests at different intensity levels were conducted, including several at the risk targeted maximum considered earthquake intensity for the building's design location. Experimental results indicate that a tall wood building with the systems and details employed in this study can withstand design basis and maximum considered earthquake level events repeatedly with no notable residual drift, no structural member or connection damage, while only experiencing moderate nonstructural damage that would be repairable, meeting the intended resilience goals. This paper provides a summary of the design, construction, testing, and primary results from this experimental program. **DOI: 10.1061/JSENDH.STENG-13752.** *This work is made available under the terms of the Creative Commons Attribution 4.0 International license, https://creativecommons.org/licenses/by/4.0/.*

Author keywords: Mass timber building; Shake table test; Resilience; NHERI TallWood; Mass timber rocking wall; Nonstructural systems.

This work is made available under the terms of the Creative Commons Attribution 4.0 International license.

Introduction

Over the past decade, notable progress has been made toward high-performance mass timber buildings through innovations in materials, components, and building systems. The recently updated International Building Code (ICC 2021) introduced new mass timber construction types that allow construction of wood buildings up to 18 stories in the United States. The ability to use a renewable and sustainable material combined with the aesthetics of exposed wood and speed of construction has resulted in strong interest in tall wood buildings. A notable portion of this potential tall wood building market is in regions with moderate-to-high seismicity such as the Pacific Northwest of the United States.

Currently, most existing tall mass timber buildings utilize a concrete core or steel braced frame as their lateral force-resisting system (LFRS) [e.g., ascent building (Gokhman 2021), Carbon12 building (Kordziel et al. 2019)]. There are two main reasons for such an approach. First, the code-accepted options in mass

[1]Associate Professor, Dept. of Civil and Environmental Engineering, Colorado School of Mines, Golden, CO 80401 (corresponding author). ORCID: https://orcid.org/0000-0002-6458-3124. Email: spei@mines.edu

[2]E.W. McKenzie Foundation Endowed Professor, Dept. of Civil and Environmental Engineering, Univ. of Nevada Reno, Reno, NV 89557. ORCID: https://orcid.org/0000-0002-0076-1630

[3]Professor, Dept. of Civil and Environmental Engineering, Univ. of Washington, Seattle, WA 98195.

[4]Harold H. Short Endowed Chair Professor, Dept. of Civil and Environmental Engineering, Colorado State Univ., Fort Collins, CO 80523.

[5]Advanced Research Manager, Simpson Strong-Tie Co., Pleasanton, CA 94588.

[6]Graduate Student, Dept. of Civil and Environmental Engineering, Colorado School of Mines, Golden, CO 80401.

[7]Design Engineer, KPFF Consulting Engineers, Seattle, WA 98101. ORCID: https://orcid.org/0000-0003-0393-379X

Note. This manuscript was submitted on February 8, 2024; approved on August 8, 2024; published online on October 12, 2024. Discussion period open until March 12, 2025; separate discussions must be submitted for individual papers. This paper is part of the ***Journal of Structural Engineering***, © ASCE, ISSN 0733-9445.

[8]Graduate Student, Dept. of Civil and Environmental Engineering, Colorado School of Mines, Golden, CO 80401. ORCID: https://orcid.org/0000-0002-0721-6264

[9]Graduate Student, Dept. of Civil and Environmental Engineering, Univ. of Nevada Reno, Reno, NV 89557. ORCID: https://orcid.org/0009-0009-6406-4269

[10]Graduate Student, Dept. of Civil and Environmental Engineering, Univ. of Nevada Reno, Reno, NV 89557. ORCID: https://orcid.org/0009-0004-6001-3070

[11]Graduate Student, Dept. of Civil and Environmental Engineering, Univ. of Nevada Reno, Reno, NV 89557.

[12]Professor, Dept. of Structural Engineering, Univ. of California San Diego, San Diego, CA 92110. ORCID: https://orcid.org/0000-0001-9109-7896

[13]Graduate Student, Dept. of Structural Engineering, Univ. of California San Diego, San Diego, CA 92110. ORCID: https://orcid.org/0000-0003-2826-9696

[14]Technical Director, KPFF Consulting Engineers, Portland, OR 97204.

[15]Professor Emeritus, Dept. of Civil and Environmental Engineering, Washington State Univ., Pullman, WA 99163. ORCID: https://orcid.org/0000-0002-1331-6923

timber-based lateral systems are still limited. In the United States, a panelized mass timber shear wall system (Amini et al. 2018; van de Lindt et al. 2020) was adopted in ASCE 7-22 (ASCE 2022) but was limited to maximum building height of 20 m (65 ft). Second, the current construction industry has familiarity with traditional steel and concrete lateral systems for tall buildings. Thus, a hybrid solution has so far been considered more economical despite the complication of mixed trades during construction. However, there are significant benefits in developing cost-effective and high-performance mass timber lateral systems for tall wood buildings, including the streamlining of the construction process (i.e., faster project delivery), the use of a sustainable material, and the added resilience against large earthquake events.

The idea of combining a mass timber lateral system with posttensioning was first explored in New Zealand (Palermo et al. 2005). The concept was used in moment frame configurations (Smith et al. 2014; Wanninger and Frangi 2016; Iqbal et al. 2016) as well as in a rocking shear wall configuration (Sarti et al. 2015; Iqbal et al. 2015). The posttensioned mass timber rocking wall was conceptualized based on previous concrete and steel rocking system research literature (e.g., Priestley 1991; Kurama et al. 1999; Deierlein et al. 2011; Wiebe and Christopoulos 2015) and offered a low-damage and potentially easy-to-construct mass timber lateral system option. There have been systematic studies on this lateral system by researchers in New Zealand (Palermo et al. 2005; Iqbal et al. 2015; Iqbal et al. 2018) and later in the United States (Ganey et al. 2017; Pei et al. 2019). Specifically, reverse-cyclic loading tests were conducted on CLT rocking walls (Ganey et al. 2017; Akbas et al. 2017) and established deformation limits for various wood damage states at the compression toe of the rocking panels. In New Zealand, Brown et al. (2021) tested a scaled four-story C-shaped CLT core wall system that was posttensioned and subjected to bidirectional loading. The tests examined screw details for the in-plane and orthogonal joints of the core wall and found that the system performed well up to 2.3% drift (the stroke limit of the test setup) with only minor damage. Amer et al. (2024) conducted biaxial tests on a scaled building system assembly to study the impact of biaxial displacement demands on rocking wall and gravity system performance. The results were used to develop fragility relationships between rocking wall damage and drift considering the impact of biaxial loading. In most of these experimental studies, this system achieved damage-free performance under design level demands and performed very well at drifts beyond design level. Notably, a handful of buildings have been designed and built using posttensioned mass timber lateral systems in New Zealand, Europe, United States, and Japan (Palermo et al. 2012; Granello et al. 2020). However, none of these exceeded five stories. In Portland, Oregon, engineers designed a 12-story office building with a mass timber rocking wall lateral system that went through the full permitting process (Zimmerman and McDonnell 2018) but was not physically built due to finance restraints.

Since the introduction of cross-laminated timber (CLT) and mass timber construction, a handful of large-scale seismic tests have been conducted on mass timber buildings where mass timber walls were used with conventional hold-down systems. Ceccotti et al. (2013) conducted tests of a seven-story CLT building at Japan's E-Defense shake table to investigate the performance of a panelized mass timber shear wall system. The test result indicated that damage was concentrated at the CLT wall hold-down connections at the foundation due to the large overturning demand generated from a multistory building, with the remainder of the building performing well other than high upper-floor accelerations. Sato et al. (2019) tested a series of three- to five-story CLT buildings in Japan, observing similar damage for large earthquakes at wall hold-down locations. In Canada, Popovski and Gavric (2016) conducted a cyclic pushover test of a two-story building featuring panelized CLT shear walls. Van de Lindt et al. (2019) tested a CLT shear wall system in a two-story building on the Natural Hazards Engineering Research Infrastructure UC San Diego (NHERI@UCSD) shake table (Van Den Einde et al. 2021), which helped contribute to a FEMA P-695 study (van de Lindt et al. 2020) that introduced CLT shear walls into U.S. building standards (ASCE 7-22). The aforementioned studies have focused on panelized shear wall systems used in platform framing configurations, which are suitable for mass timber buildings with compartmentalized floor plans. While more robust than the traditional light-framed wood shear wall system, platform-framed mass timber shear walls typically experience damage and failure at wall-to-diaphragm and interpanel connections under strong earthquakes in order to achieve ductility and energy dissipation. The need to repair or replace these connections after strong earthquakes limits the resilience of such buildings. In 2017, Pei et al. (2019) conducted shake table tests on a two-story full-scale specimen with a posttensioned CLT rocking wall system, with supporting numerical modeling by Wichman et al. (2022) and demonstrated its structural resilience under uniaxial earthquake excitation. Another rocking wall system with sacrificial compression blocks was also tested on the same two-story building configuration by Blomgren et al. (2019) and performed quite well. These early tests provided confidence to scale up the application of mass timber rocking walls in taller buildings.

Building on these previous efforts, the test program presented here is part of a National Science Foundation (NSF) sponsored research project aimed at developing and validating a resilience-based seismic design methodology for tall wood buildings. Coined the NHERI TallWood Project, central to this effort was the design, construction, and testing of a full-scale 10-story mass timber building with a posttensioned mass timber rocking wall lateral system,

Fig. 1. Full-scale 10-story NHERI TallWood test structure with rocking wall lateral system. (Image by authors.)

This work is made available under the terms of the Creative Commons Attribution 4.0 International license.

a low-damage gravity framing system, and drift compatible nonstructural systems. The test building represents an archetype that is suitable for mixed-use, tall, mass timber buildings in high seismic regions. The 10-story test building was partially finished with interior partition walls and exterior façades, and egress and ingress were facilitated with a full-scale prefabricated stair system. These nonstructural assemblies were specifically detailed to limit earthquake-induced damage. The large outdoor shake table at NHERI@UC San Diego is the only facility in the world where a full-scale 10-story building specimen can be tested because it imposes no height limit for the specimen. To date, this test structure represents the tallest full-scale building structure ever tested on a shake table (see Fig. 1). The design, construction, testing, and major findings from the NHERI TallWood shake table test program are presented in the following sections. For clarity, information on the structural system design and response is presented first, followed by a high-level summary of nonstructural and stair system configurations and performances.

Test Building Design

Gravity System Design

The building footprint was constrained to a size that could be supported by the shake table platen, which is 7.6×12.2 m (25×40 ft). While there is no height limit, the height of the building was constrained to be within a reasonable proportion to the floor plan dimensions. Based on these physical constraints, the test building floor plan and elevation were sized as shown in Fig. 2 (the *X*-*Y* axis of the shake table facility is also shown). A single floor area was 84 m^2 (900 ft^2) and was uniform over the building's height. The total building height was 34.4 m (113 ft). The column grid consisted of 14 gravity columns arranged within the space limitations of the shake table surface. Cantilevered precast concrete foundation blocks were used to expand the surface of the shake table so that the building's first floor plan included cantilevered patio portions toward the north and south directions beyond gridlines A and D, which supported four different types of exterior nonstructural façades.

During the design process, the gravity frame members (LVL beams and columns) were sized first using a typical loading scenario for office space [i.e., 3.3 kN/m^2 (70 psf)] for dead and 3.1 kN/m^2 (65 psf) for live loads. The columns and beams were sized for a 2 h fire rating based on fire design requirements from the National Design Specification for Wood Construction (NDS, AWC 2018), which added about 50 mm (2 in.) of thickness for mass timber members on all exposed sides. Fire design was specifically implemented for the test building to represent realistic column and beam sizes for connection detailing, as many wood beams and columns will be exposed in such buildings. A uniform cross section was used for beams and columns to simplify fabrication and column splice design (member sizes could vary in a real building project for cost savings). Similarly, structural strength or stiffness

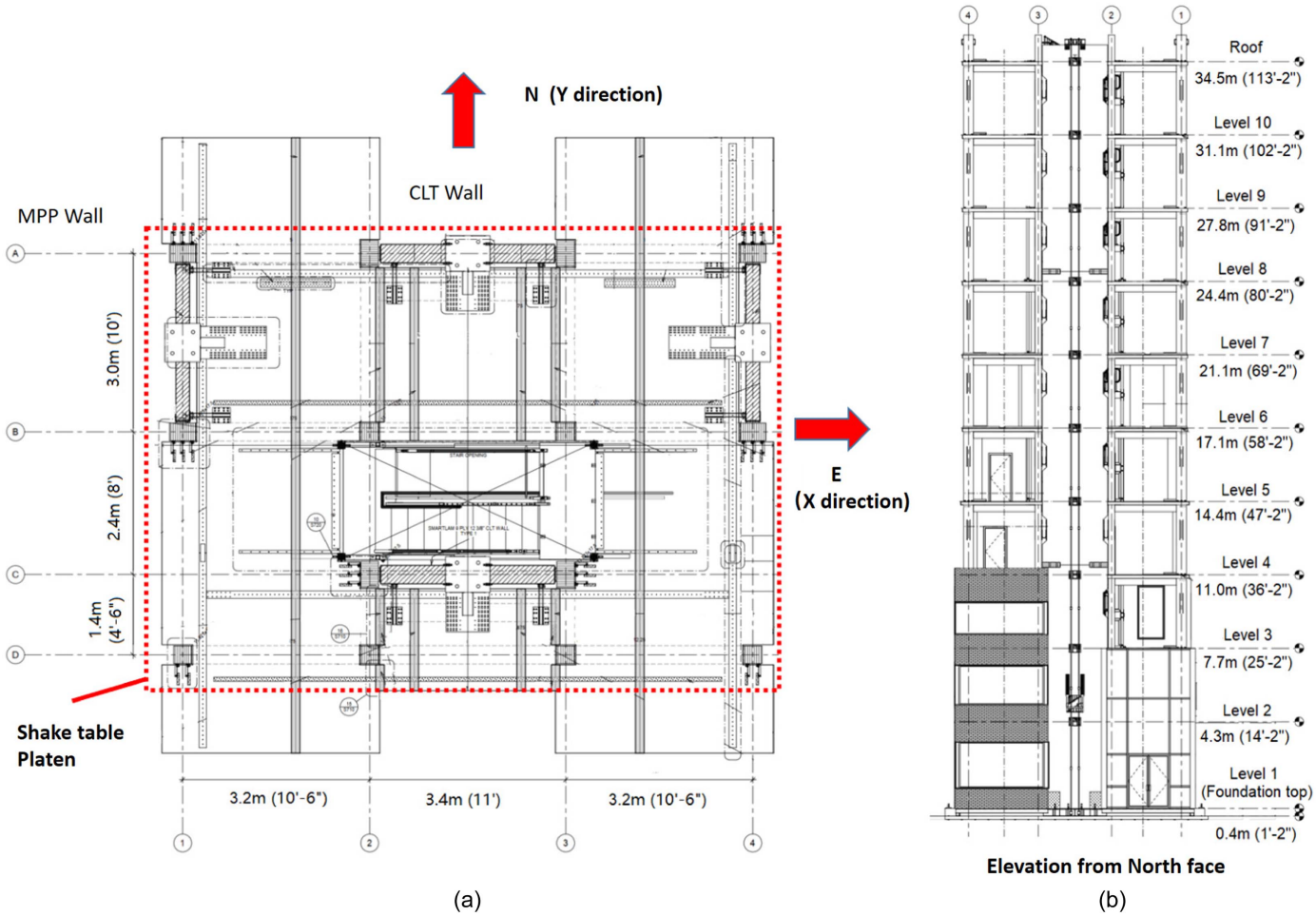

Fig. 2. Test specimen schematic: (a) plan view of typical floor; and (b) elevation view.

This work is made available under the terms of the Creative Commons Attribution 4.0 International license.

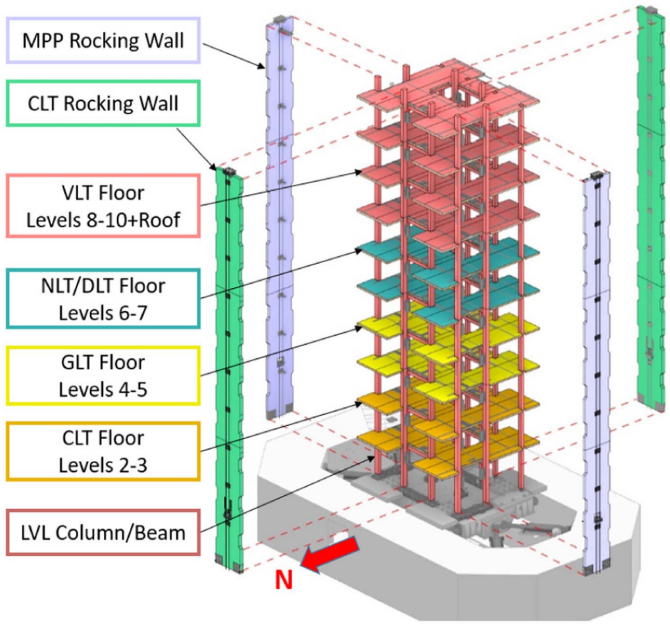

Fig. 3. Mass timber structural elements (graphic courtesy of LEVER Architecture; see Table 1 for material acronyms).

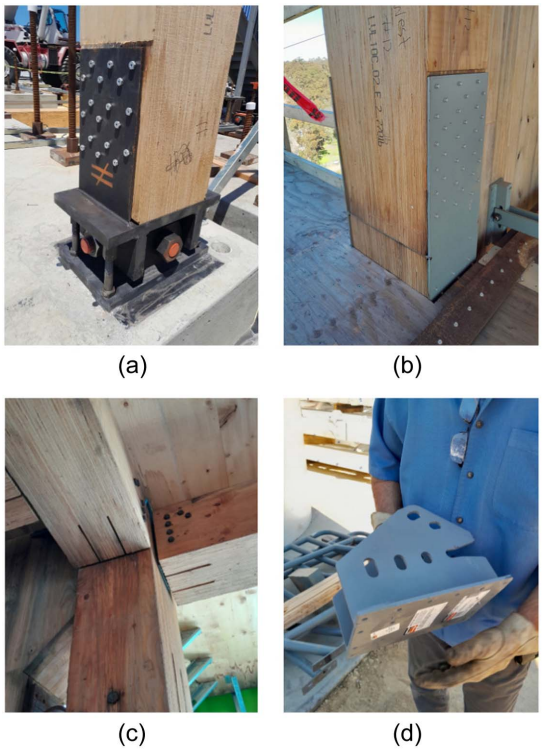

Fig. 4. Gravity frame connection details: (a) column base connection; (b) column splice connection; (c) beam and column joint; and (d) special beam hanger. (Images by authors.)

was not the controlling criteria for the selection of the floor panel thickness in this study. As shown in Fig. 3, multiple types of mass timber products were used for the floor diaphragms to test the feasibility of different products. Five-ply CLT panels were selected for Floors 2 and 3 to provide adequate fire resistance of a diaphragm with an exposed ceiling. On the remaining floors, other mass timber floor systems were selected to have similar thicknesses as the CLT floors for similar fire resistance and detailing. The bounding columns, located on each side of the rocking walls, had larger cross-sections than typical columns to resist axial forces generated from the steel yielding energy dissipation devices [U-shaped flexure plates or UFPs were used in this test for its cost-effectiveness and reliability, but other type of energy dissipation devices could also be used (Skinner et al. 1974)]. The gravity and lateral system materials and dimensions are summarized in Table 1 and illustrated in Fig. 3, including the four mass timber rocking walls shown in exploded view for clarity.

To achieve damage-free performance under repetitive earthquake tests, connections for the gravity system in the test building were specially designed by an industry partner to allow free rotation up to 5% interstory drift while providing adequate axial stiffness and strength for column bracing (Pryor et al. 2024). Examples of these connection details can be found in Fig. 4(d), with detailed structural drawings available in Busch (2023). The column base was detailed as a true pin to allow biaxial rotation [see Fig. 4(a)]. While such a column base would not be required even in a resilient mass timber building, it was necessary for this study to ensure the columns were not damaged for many phases of testing by multiple research teams. The column splices were located at the floor levels and were designed for axial loads from gravity. Bounding column splices were also designed for a net tension force demand generated from a subsequent project to NHERI Tallwood, which reused the 10-story specimen. The beam-to-column connection used a beam hanger with slotted holes that transferred shear but permitted rotation about a top bolt to minimize moment transfer. The beam hanger was embedded within the wood for fire protection of the steel components.

Lateral System Design

The design of the building's lateral force-resisting system was intended to limit structural and nonstructural component damage by controlling the drift of the building. An in-depth description of the design of the lateral force resisting system can be found in Wichman (2023) from preliminary design to performance verification using nonlinear response history analysis as well as the

Table 1. Dimensions and properties of mass timber structural components

Building component	Material	Grade/Species	Cross-Section dimensions
North/south rocking walls	Cross laminated timber	2400-2.0E/Southern Pine	314 mm (12.37 in.)
East/west rocking walls	Mass plywood panel	F16-9/Douglas Fir	233 mm (9.19 in.)
Beams and columns	Laminated veneer lumber	Custom/Douglas Fir	302 × 311 mm (11.87 × 12.25 in.)
Bounding columns[a]	Laminated veneer lumber	Custom/Douglas Fir	302 × 445 mm (11.87 × 17.50 in.)
Diaphragm Level 2-3	Cross laminated timber	Custom/European Spruce	180 mm (7.09 in.)
Diaphragm Level 4-5	Glulaminated timber	Custom/European Spruce	156 mm (6.12 in.)
Diaphragm Level 6-7	Nail/dowel laminated timber	Custom/Douglas Fir	152 mm (5.98 in.)
Diaphragm Level 8-10 and roof	Veneer laminated timber	Custom/Douglas Fir	162 mm (6.38 in.)

[a]Bounding columns are the eight columns located on each side of the rocking wall panels.

This work is made available under the terms of the Creative Commons Attribution 4.0 International license.

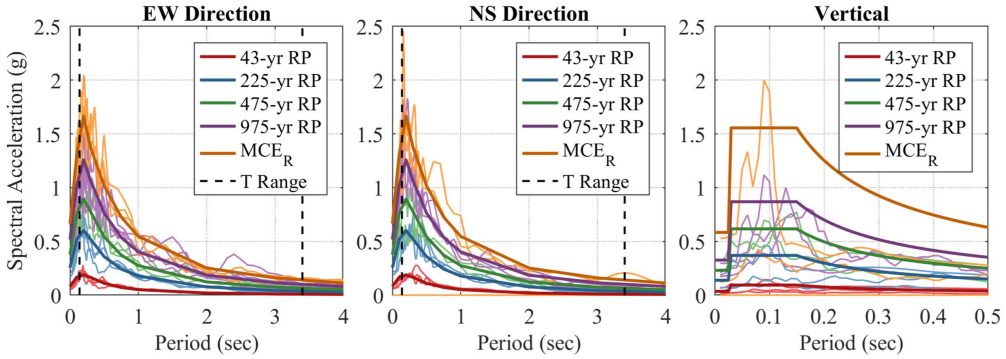

Fig. 5. Response spectrum at the different hazard levels considered for design and implemented in testing. (Data from Wichman 2023.)

Table 2. Resilience design objectives of the test building

Hazard return period (yr)	225 & below	475	975	MCE_R
Lateral system	No damage[a]	No damage	No damage	Repairable damage
Gravity system	No damage	No damage	No damage	No damage[d]
Nonstructural system	No damage	Minor damage[b]	Repairable damage[c]	Repairable damage

[a]Maximum interstory drift <0.50%.
[b]Maximum interstory drift <1.00%.
[c]Maximum interstory drift <2.25%.
[d]Gravity system for this building was designed to remain damage-free under MCE_R level demands strictly to support the desired test program, which involves repetitive MCE_R level shakes.

calculation of demand-to-capacity ratios for all limit states of the walls and connections. A brief summary is provided in the following.

The building was designed for a location in Seattle, Washington, on Site Class C soil. The ATC hazards by location tool (ATC 2021) was used to generate short period (S_{MS}) and 1 s (S_{M1}) risk targeted maximum considered earthquake (MCE_R) spectral acceleration values of 1.65 and 0.72 g, respectively. Uniform hazard spectra (UHS) were also generated for several different hazard levels (i.e., return periods [RP]), as shown in Fig. 5. The seismic hazard in Seattle is unique in that there are significant contributions from crustal faults and the Cascadia Subduction Zone (producing interplate and intraplate earthquakes). The UHS were developed using the USGS 2014 US earthquake source model (USGS 2017a) and generated for a site with a time-averaged shear-wave velocity to 30 m depth (V_{S30}) equal to 500 m/s (using USGS 2017b). The site-specific MCE_R spectrum was also developed per ASCE/SEI 7-16 Section 21.2.1.1 (ASCE 2016) and is as shown in Fig. 5. The target vertical acceleration spectra were developed in accordance with Section 11.9 of ASCE/SEI 7-16, which is typically used for defining the MCE_R vertical spectra. For other hazard levels, that same procedure was used but with S_{MS} replaced by the 0.1 s horizontal spectral acceleration from the various UHS given in Fig. 5.

With the hazard levels defined, desired maximum damage states for the structural systems and connections were selected for each hazard level and then the maximum drift limits corresponding to the damage states were assigned. The maximum drifts corresponding to each damage state were determined based on experimental data (Wichman et al. 2022), detailed analyses of specific components (e.g., the gravity frame connections), or engineering judgment from past wood building fragilities. The drift targets also served as a key design constraint (2.5% limit was used in the design stage) for the nonstructural systems, including the façades, interior walls, and stairs, which are described in later sections and detailed in Roser et al. (2024), Wynn et al. (2024), Ji et al. (2024), and Sorosh et al. (2024). While it is the first time most of these nonstructural systems were tested under 3D motions in a full-scale building setting, the research team collaborated with experienced industry partners to meet these target damage states (which were later validated). The design objectives for the test building at different hazard levels are summarized in Table 2. Note the no-damage designation for energy dissipation elements corresponding to no fracture or visible cracking of such elements. These elements will experience yielding and nonlinear response as they deform. It should also be noted that the low-cycle limits for UFPs developed in Skinner et al. (1974) were used to inform the UFP radius design.

The lateral system consisted of two pairs of posttensioned rocking walls: one pair constructed using CLT panels; and the other using mass plywood panels (MPPs). Two materials were used to demonstrate the versatility of the design approach regardless of the mass timber product used. The seismic weight of the building was estimated (see Table 3) as 277 metric tons (611 kips). Rocking wall parameters were first determined using a prescriptive design method developed by the project team and industry collaborators (Busch et al. 2022). This method applied modal response spectrum analysis with an elastic model of the walls, using the site's seismic hazard and an assumed seismic force reduction factor, R, of 6 to obtain initial wall dimensions and thickness, posttensioning sizes and initial stressing, and energy dissipation capacities and distribution.

Table 3. Seismic weight distribution on each floor and roof

Floor	Mass (Metric ton (kip))	Floor	Mass (Metric ton [kip])
2	34.6 (76.3)	7	23.9 (52.6)
3	30.4 (67.0)	8	30.0 (66.2)
4	34.4 (75.8)	9	25.0 (55.2)
5	25.1 (55.4)	10	24.9 (54.9)
6	24.9 (54.8)	Roof	23.9 (52.7)

This work is made available under the terms of the Creative Commons Attribution 4.0 International license.

Note this value of R is slightly less than the value of 7 recommended in Sarti et al. (2017) and therefore slightly conservative relative to those recommendations.

Following the initial design, the lateral force-resisting system was checked and refined using the performance-based design methods outlined in the LA Tall Building Guidelines (LATBDC 2023), which are often adopted for tall buildings in urban areas of the West Coast. This process included the development of an OpenSees (Mazzoni et al. 2006) model for nonlinear response history analysis as described in Wichman (2023). The analyses used suites of ground motions selected and scaled to match the intended hazard levels and representative of the source characteristics of the hazard at the building's design location (i.e., the suites at each hazard level contain records from crustal, interplate, and intraplate earthquakes in relative quantities consistent with the source contribution to each hazard level). The ground motions were selected and scaled over the period range illustrated in Fig. 5, consistent with the requirements of ASCE 7-16. Following the LA Tall Building Guidelines, 1.3 times the suite mean and 1.0 times the suite maximum demands from MCE_R hazard level simulations were checked against force-controlled actions (i.e., component strength limit states) and suite mean and suite maximum component deformations were checked against selected deformation limits for deformation-controlled actions. Additionally, the distributions of the suite mean story drifts at other hazard levels were also computed and compared with the design targets in Table 2. The final wall design parameters are provided in Table 4, and the final configuration is shown in Fig. 6. A detailed engineering drawing set for the as-designed building can be found in Busch (2023).

Detailed design calculations for all components and connections of the rocking wall lateral system can be found in Wichman (2023). The rocking walls were allowed to reach strains above yield but below crushing for the MCE_R demands such that the building could be reused for subsequent research projects. Other components were designed at MCE_R using limit states derived from the NDS (AWC 2018) for timber components and AISC 360-16 (AISC 2016) for steel components.

Lateral load transfer from the diaphragm to the rocking wall was achieved using a shear key detail shown in Fig. 7. This connection detail was adopted from an earlier shake table test (Pei et al. 2019; Blomgren et al. 2019) because it demonstrated resilient performance with no damage to the diaphragm, walls, or steel components. The vertically slotted connection in the rocking wall panel allowed the wall to move independently from the diaphragm in the vertical direction, decoupling the rocking walls from the gravity load-bearing system. The connection between the shear key and the floor diaphragms varied depending on how diaphragm shear was developed for the different mass timber panel materials used. For diaphragms without plywood sheathing (CLT and VLT), a concentrated wing-plate with 45-deg screw connections was used. For floors with plywood sheathing (glulaminated timber, nail laminated timber, and dowel laminated timber floors), a different connection detail was adopted so that the shear would be effectively transferred into the sheathing layer. The rocking walls were braced out-of-plane to the diaphragm at all floor levels using a connection designed to resist tension and compression forces while still allowing vertical wall movement relative to the floor. The demand for the wall lateral braces was estimated using the lateral bracing requirements for point bracing of members in combined bending and axial compression from AISC 360-16 (AISC 2016). Photos for these connection details are presented in Fig. 7.

Due to the relatively small footprint of the building, the floor diaphragms were designed and modeled as rigid. The lateral force demands for the diaphragms were obtained from the nonlinear time history analysis following the LA Tall Building Guidelines. The design objective was to keep the diaphragm damage-free during all tests. Similarly, the diaphragm chords and shear straps were designed to remain elastic. On the sheathed floors, NDS SDPWS (AWC 2021) high-capacity diaphragm design provisions were followed. The diaphragm design demands were largest in the upper levels, which had the largest floor accelerations from the nonlinear analyses.

Construction Process

Before construction started, the foundation blocks (the precast concrete blocks used to support gravity columns and nonstructural walls) were installed on the shake table to expand the table surface to accommodate the building floor plan. Custom steel beams were used as the foundation element of the rocking walls for ease of installation and anchoring. All foundation elements were anchored to the shake table through posttensioned anchor rods, thus becoming a

Table 4. Rocking wall design parameters

Wall component	CLT rocking wall	MPP rocking wall
Wall Dimensions	Cross section size 314 × 2,975 mm (12.375 in. × 9 ft.–9.125 in.) Three wall segments heights 11.13, 13.41, and 10.36 m (36 ft-6 in., 44 ft, and 34 ft)	Cross section size 233 × 2,670 mm (9.1875 in. × 8 ft–9.125 in.) Three wall segments heights 11.13, 13.41, and 10.36 m (36 ft-6 in., 44 ft, and 34 ft)
Wall grade	Major lams: 2400-2.0E Minor lams: Southern Pine, No. 1	Freres Lumber: F16-9
Post-tensioning (PT) rod	Four PT rods per wall, each rod posttensioned to 222 kN (50 kips), approximately 49% of yield. (based on ATS-HSR10) Each rod diameter is 50.8 mm [2 in., ATS-HSR16 from Simpson Strong-Tie (Pleasanton, California)] up to Level 2, then rod diameter is reduced to 31.8 mm (1.25 in., ATS-HSR10) from Level 3 to roof. Fy = 724 MPa (105 ksi)	
UFP	203 mm (8 in.) wide steel plates bent into a 171 mm (6.75 in.) diameter half circle with leg length of 222 mm (6.75 in.) from where the curvature ends to the to the first bolt. Two thickness values were used Type 1: 9.5 mm (3/8 in.) Type 2: 12.7 mm (1/2 in.) Each rocking wall has 14 Type 1 UFPs and 12 Type 2 UFPs	

This work is made available under the terms of the Creative Commons Attribution 4.0 International license.

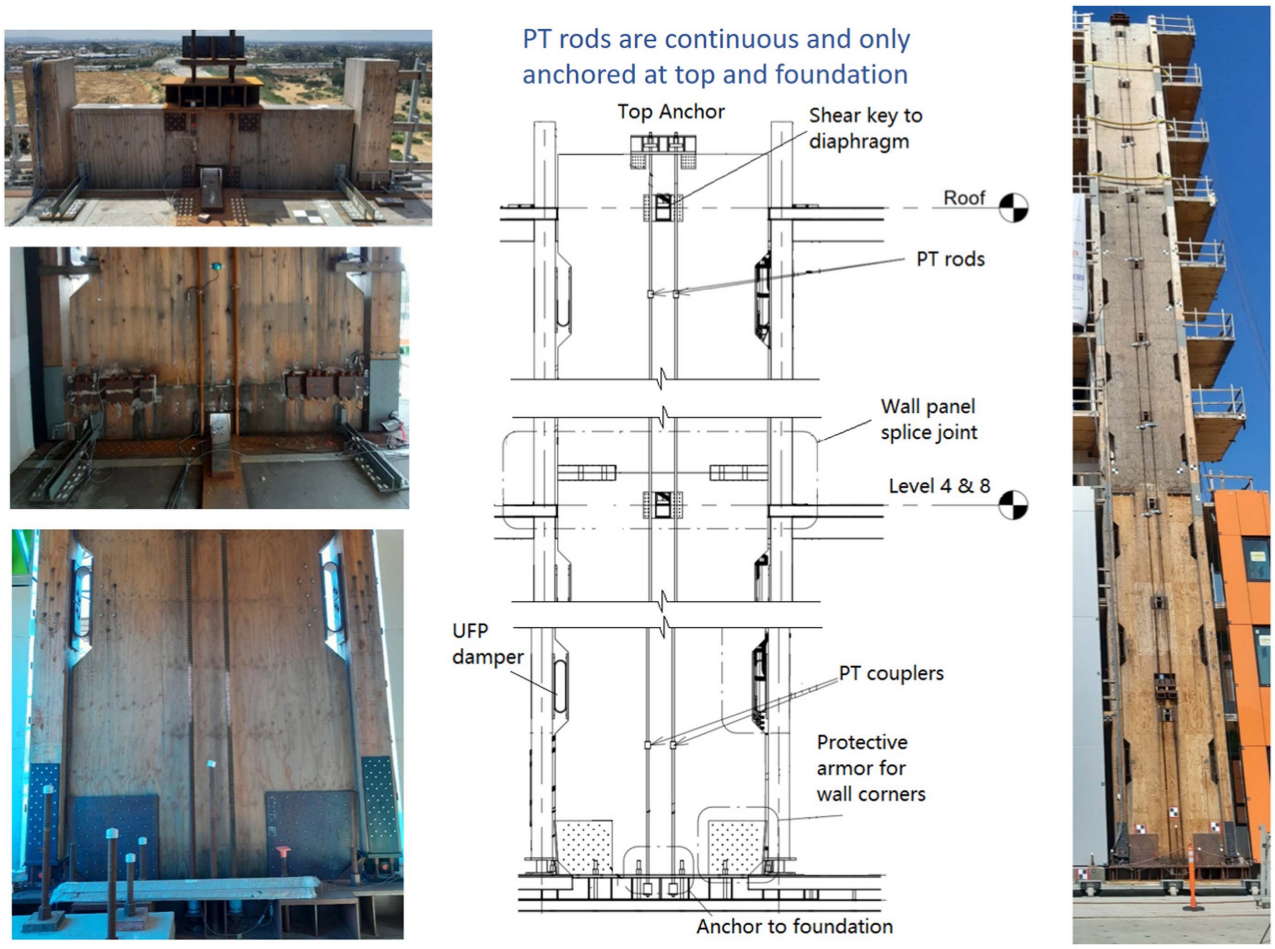

Fig. 6. Key components and sections of rocking wall system. (Images by authors.)

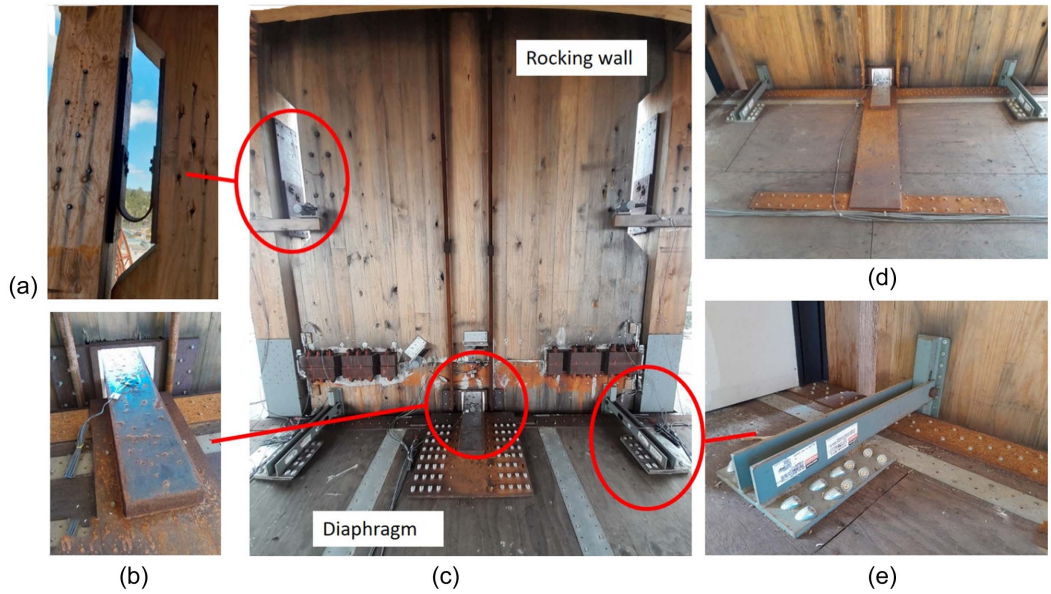

Fig. 7. Connections for the lateral force resisting system: (a) UFP between wall and bounding column; (b) shear key wall-to-diaphragm connection; (c) typical wall-to-diaphragm connection interface showing nonsheathed floor wing plate; (d) alternative wing plate connection detail for sheathed floors; and (e) out-of-plane brace for rocking wall. (Images by authors.)

This work is made available under the terms of the Creative Commons Attribution 4.0 International license.

Fig. 8. Structural construction sequence of the test building. (Images by authors.)

rigid part of the steel shake table platen. After the foundation was ready, the structural construction of the building was completed with a relatively small crew (four to six carpenters depending on the labor demand each day) in approximately 2.5 months. The actual structural construction spanned more than four months due to a 1.5-month inactive waiting period for needed parts. The installation of nonstructural wall assemblies lasted for about four months, including some time-overlap with structural construction. The stair tower was assembled in parallel with the structural construction. Overall, construction started in mid-July 2022 and concluded in February 2023.

The first three levels of the stair system and gravity columns were installed on the foundation blocks, followed by the installation of beams, floor panels, and the first segments of rocking wall panels. As shown in Fig. 8, the first gravity column segments and rocking wall panel segments were both three stories tall. After the first segments of wall panels were in place, temporary posttensioning anchors were installed at the second story of each wall panel to provide temporary lateral support for stability and wind loading resistance during construction. This detail would not be necessary for full-sized building projects where the floor diaphragms are large enough to accommodate temporary braces for construction stability. After reaching Level 4 and completing the posttensioning of the first wall segments, a similar sequence was repeated for the next two segments (stories four to seven and stories eight to ten). Wall segments were spliced together vertically at their interfaces above levels 4 and 8. After topping out the building, posttensioning rods were installed for the full height of each rocking wall with the design PT forces. The temporary construction posttensioning at the middle of the first panel segment was released at the same time.

One of the major challenges in structural erection was splicing the rocking wall panels on site. With the increasing span and height of mass timber structures, efficient and reliable splicing details for mass timber panels are critical for construction efficiency and economy of mass timber projects. Specifically, the rocking wall panel splices in this project needed to remain stiff and elastic throughout the entire test program, with the capability to fully transfer all flexural and shear demands from the seismic loading across the splices. A glued-in rod detail (i.e., threaded steel rods epoxied into long holes drilled into the end of each wall segment) was designed for this connection similar to a connection that had been used successfully on past projects (Zimmerman et al. 2021). The glued-in rod connections used development lengths for the flexural rods and shear capacities for the shear rods determined from independent testing at Oregon State University (Field et al. 2023). However, a hand-fabrication method used by the fabricator to predrill the splice rod holes resulted in errors in location of the holes that prevented alignment of the wall segments onsite. The research team developed an alternative design for the tensile region of the splice and enlarged the holes in the shear region to enable the splicing of the wall panels. Customized steel coupler plates were installed at each corner of each wall panel such that the epoxied rods from each wall segment were connected to a steel plate coupler; then, the coupler plates were bolted together from the outside of the panel. Despite this fabrication error, the adjusted splice design successfully transferred the large tension forces from flexure across the wall segments using long glued-in threaded rods as intended. Fig. 9 shows the component details from the final wall splice and its assembly. A detailed description of the construction challenges associated with the wall splice can be found in Busch (2023); detailed calculations for the original and modified splice designs can be found in Wichman (2023).

This work is made available under the terms of the Creative Commons Attribution 4.0 International license.

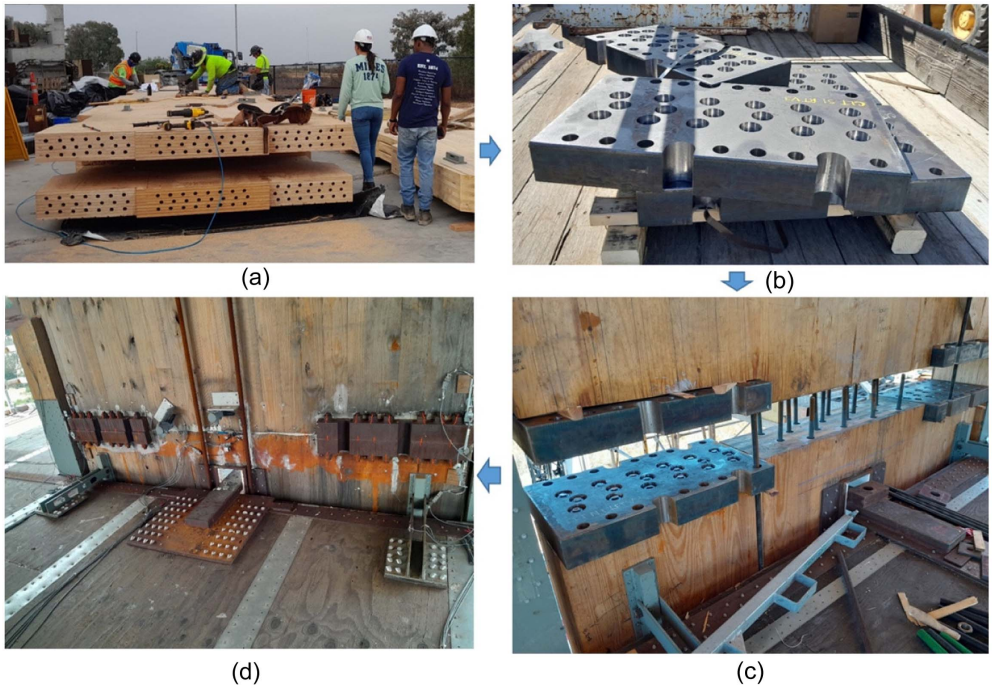

Fig. 9. Wall panel splice joint detail: (a) notched panel interface with epoxy holes; (b) coupler plates; (c) installation of a panel splice onsite; and (d) completed panel splice. (Images by authors.)

Instrumentation Plan

The test building was instrumented heavily with over 700 channels of sensors for structural and nonstructural measurements. In addition, more than 40 high-resolution GoPro and IP video cameras were installed in and around the building to provide visual documentation of the building component responses. The sensors were installed in key locations on the building to achieve the following objectives:

1. Record building global responses, including acceleration and displacement of each floor.
2. Monitor force and deformation demands in structural components such as the rocking walls and various connections within the lateral and gravity force-resisting systems.
3. Measure nonstructural component accelerations and deformations across movement joints.
4. Generate video footage data for validation of building component interaction and movement assumptions.

A summary list of the sensors is presented in Table 5. Fig. 10 shows typical sensor types installed in the building as discussed here. Detailed drawings and a comprehensive list of sensors on the building can be found in Busch (2023). A summary of the plan and rational for installed structural sensors on different building components is also presented here.

Table 5. Summary of instrumentation channels deployed on the TallWood test building

Building component	Sensor types[a]	Total number
Global displacement	SP, AC, GPS	139
Gravity system	LP, SP	79
Rocking walls	LC, AC, TL, SG, SP	196
Nonstructural walls	AC, SP, LP	186
Stairs	AC, SP, LP, SG	109

[a]SP = string-potentiometer; AC = accelerometer; LC = load cell; LP = liner-potentiometer; TL = tilt meter; SG = strain gauge; and GPS = high-precision GPS.

Global building responses: Accelerometers were installed on the floor diaphragms to measure floor accelerations. One triaxial accelerometer was installed at the center of mass location of each floor, with additional accelerometers at other locations to measure torsional and vertical floor responses [Fig. 10(c)]. On most levels, diagonally oriented string-potentiometers (string-pots) were installed between floors in both directions to measure interstory drifts [Fig. 10(d)]. At lower floors, string-pots were also installed between the building and safety towers (fixed on the ground outside of the moving shake table platen) to measure absolute building displacement. At higher floors, where a fixed reference measurement is not possible, eight high-precision GPS units were installed to capture absolute displacement and velocity [Fig. 10(c)].

Gravity frame: Instrumentation for the gravity system was focused on beam and column connections and relative movement between column and floor panels. As noted, gravity frame beam-to-column connections were designed to be able to rotate freely during earthquakes. Linear potentiometers were installed to measure the deformation and rotation demands at these joints. While relative slip at the beam-to-floor interface and at column splices was intended to be prevented by design, linear potentiometers were installed to monitor these details as well.

Rocking wall system: The posttensioned rocking wall system was also heavily instrumented. Accelerometers and tilt-meters [Fig. 10(b)] were attached at selected floors on the CLT and MPP rocking walls. Linear potentiometers were placed at wall panel splice joints to monitor deformation at the splice and near the rocking interface at the base to monitor uplift and/or compressive deformation [Fig. 10(f)]. String-pots were used to measure UFP deformation [Fig. 10(e)] and the movement of the shear key connection from the floor to the wall. Commercial and custom load cells were installed on PT bars to monitor the force variation during tests [e.g., Fig. 10(a)]. Strain gauges were used to estimate the stress and force level in the shear key components and out-of-plane wall braces.

This work is made available under the terms of the Creative Commons Attribution 4.0 International license.

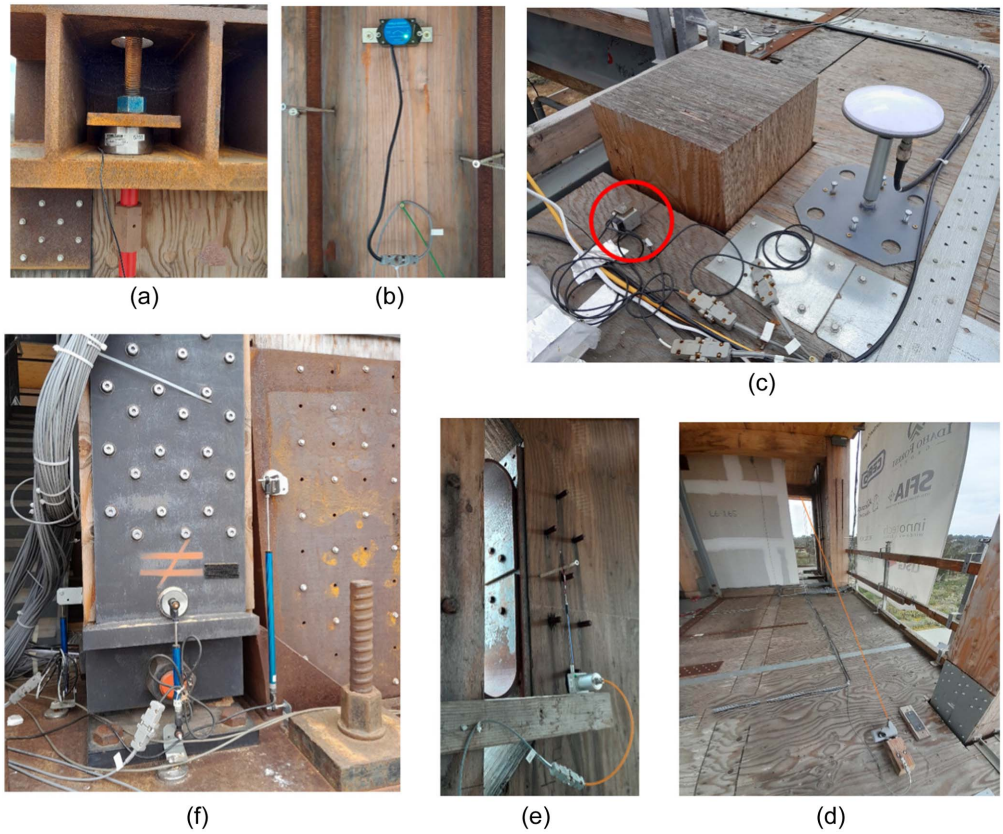

Fig. 10. Example sensors installed on the building: (a) load cell for PT force; (b) tiltmeter on rocking wall; (c) accelerometer (circled) and high precision GPS; (d) diagonal string-pot for interstory displacement; (e) string-pot for UFP displacement; and (f) linear potentiometers for column rotation and rocking wall uplift. (Images by authors.)

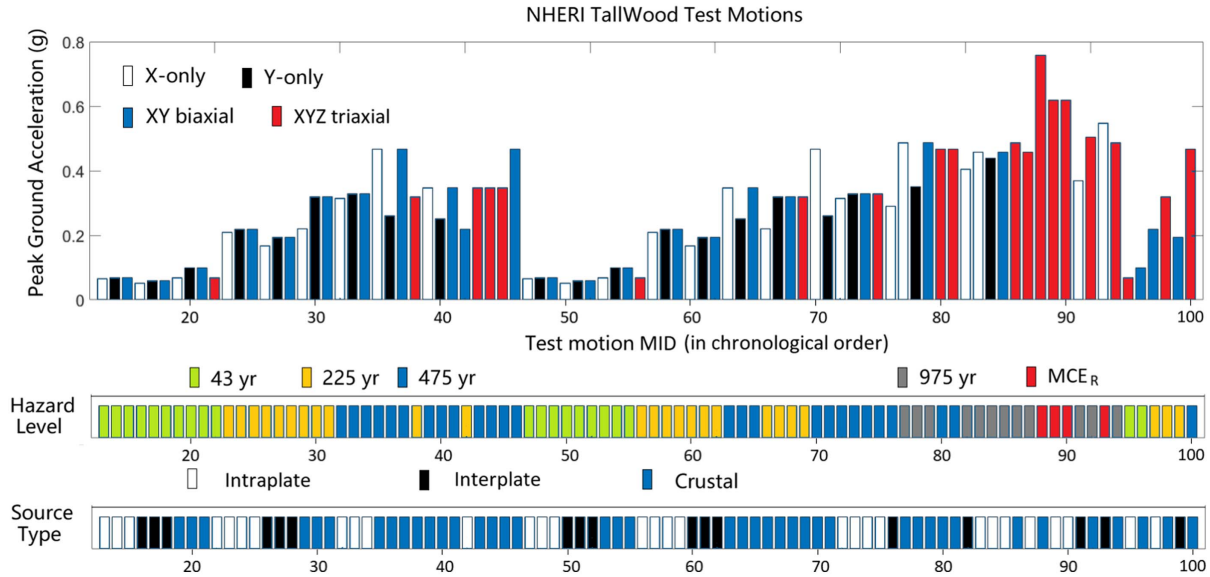

Fig. 11. NHERI TallWood test plan (PGAs shown for multidirectional tests were the maximum of the horizontal motions).

Test Program

The overarching focus of the test program was to validate the resilient performance of the building. Thus, the test ground motions and their scale factors were selected from the suites of motions used in the design (Wichman 2023). The test plan incorporated motions from the five different hazard levels with the target spectra as shown in Fig. 5. A total of 88 dynamic tests using the selected ground motions were conducted over a three-week period. The target test intensities (shown as maximum horizontal peak ground acceleration

This work is made available under the terms of the Creative Commons Attribution 4.0 International license.

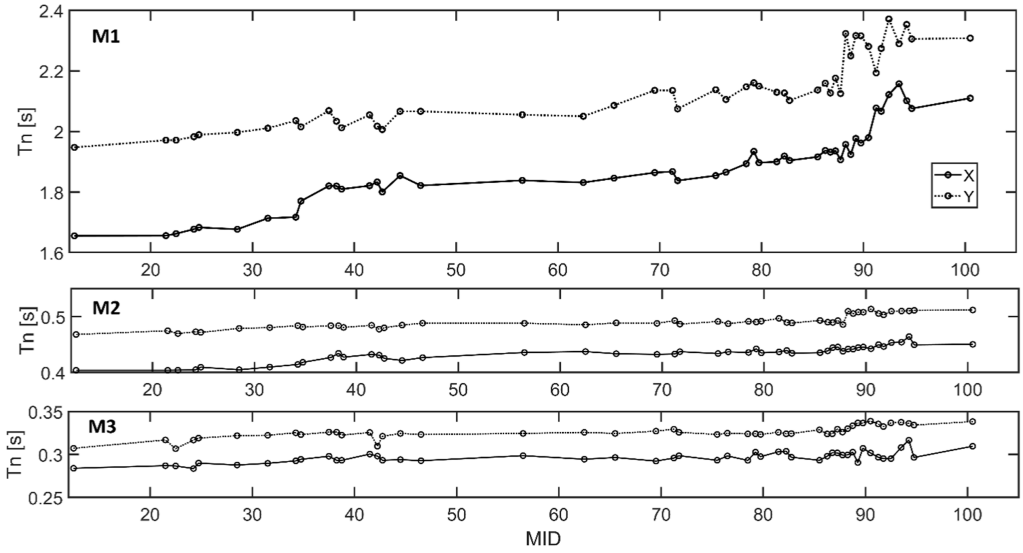

Fig. 12. Natural periods of first six modes estimated through white noise results (M1, M2, and M3 correspond to the first, second, and third translational modes).

[PGA]), hazard levels, source types, and ground motion directions are illustrated in Fig. 11 in chronological order. The ground motion ID (MID) starting with MID13 and ending with MID100 correspond to the numbering scheme used in the original raw data set. White noise tests with a 4% g root mean square (RMS) magnitude and 60 s duration are not shown in this figure but were conducted between major tests in each of the X (EW) and Y (NS) directions separately to monitor the potential change in the building's natural periods.

Fig. 12 illustrates the change in monitored natural periods of the building in X and Y directions estimated based on white noise responses. In order to demonstrate the relationship between the test program progression and change in building dynamic characteristics, natural periods of the first three translational modes were plotted against the same MID numbering system as in Fig. 11 (e.g., period estimated from WN tests after MID-X are plotted at MID-X location). Initially, the observed natural periods agreed relatively well with the numerical model used for the design and analysis of the building [fundamental period estimated form numerical model was 1.74 s; see Wichman (2023)] but was larger than the period estimation from ASCE/SEI 7-16 simplified formula (i.e., 0.69 s). As shown in Fig. 12, repetitive tests at lower and moderate intensity levels did reduce the stiffness of the building gradually. After a few MCE_R tests (starting from MID 88), more significant deterioration of the building's first mode periods from WN measurements was observed in the X and Y directions. This is likely due to damage and softening in the nonstructural systems attached to the structure as well as localized crushing of the mass timber panel corners at the base (see Fig. 13). Such localized damage did not affect recentering ability or strength of the lateral system but did cause reduction in rocking wall initial stiffness.

During the test program, critical building responses were measured and compared with the simulation results in Wichman (2023) to ensure safety of the test program. In summary, the test program of NHERI TallWood project included 21 × 43-year return period (RP) earthquakes, 25 × 225-year RP earthquakes, 26 × 475-year RP earthquakes, 12 × 975-year RP earthquakes, and three earthquakes at MCE_R (note that MID89 in Fig. 11 did not achieve the intended hazard level due to inadequate shake table pressure).

Structural Response Overview

After 88 earthquake tests, the building remained plumb with no detectible residual drift. Detailed inspections were conducted after major tests, and no visible damage was found in any structural components. The building clearly exhibited the participation of higher modes during dynamic excitation, which was visible to on-site observers even during low intensity earthquakes and white noise tests. This phenomenon will be discussed in detail later in this section. Overall, the performance of the building satisfied and exceeded the design expectations outlined in Table 2.

With the building's resilient performance, it was possible to perform multiple tests at each hazard level to collect building response

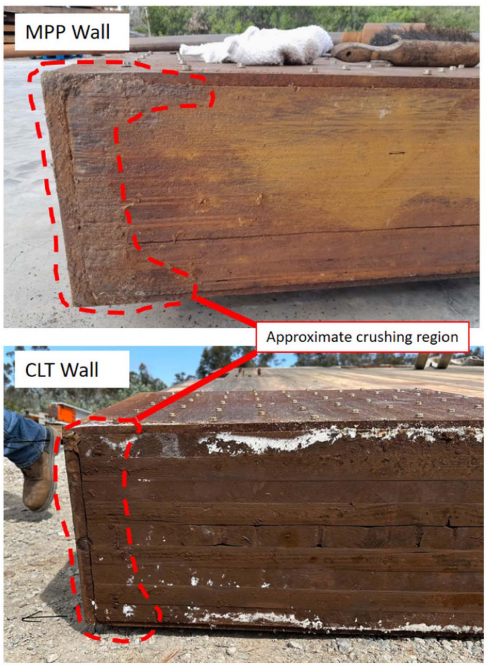

Fig. 13. MPP and CLT rocking wall toe area detail observed after deconstruction. (Images by authors.)

This work is made available under the terms of the Creative Commons Attribution 4.0 International license.

data repetitively. These data points can be used to construct a probabilistic distribution for engineering demand parameters (EDPs, such as maximum drift) of interest at each hazard level. Interestingly, this process mimics the typical performance-based seismic simulations in which conditional distributions (i.e., fragility curves) of EDPs are developed numerically through simulations. In the following sections, key response quantities from the tests are presented followed by the presentation of experimentally obtained seismic fragility curves for various EDPs.

Floor Displacements and Acceleration

With multiple accelerometers installed at each floor, acceleration records at the floor center of mass (COM) location can be extracted. In this study, the recorded acceleration was filtered with a fourth-order Butterworth bandpass filter with cutoff frequencies of 0.1 and 50 Hz. The filtered acceleration was then integrated, filtered again, and integrated again to obtain absolute displacements. In most cases, accelerometers located at the approximate center of mass were used for displacement and drift calculations. When certain center of mass accelerometers experience malfunction, other nearby accelerometers were used. Note that no significant torsional response was measured or observed during the tests. String-pot displacement data between floors and relative to fixed safety towers (available at lower floors) was also used to cross-check and verify the displacement results obtained through double integration.

The peak interstory drift and floor accelerations from all tests, grouped according to the predefined target hazard levels, are plotted in Fig. 14 as empirical cumulative distribution curves for each hazard level. A fitted lognormal distribution model is also shown. The bar chart at the bottom of Fig. 14 indicates the floor levels at which the peak drifts/accelerations were observed. The data indicate that peak interstory drift of the building at MCE_R level excitations averaged about 2%, which is in good agreement with the intended design target. The overall peak drift (2.4% at Story 7) occurred during MID 91, which was a uniaxial interplate subduction zone earthquake record from the 2011 Tohoku Earthquake applied in the X direction. Across the entire test sequence, the overall maximum floor acceleration of 2.07 g was observed on Floor 7 during MID 90, which was a MCE_R-scaled 3D intraplate earthquake motion. In general, the peak interstory drift for a given test tended to be observed within one of the top four floors, while the peak accelerations occurred mostly at midheight or the roof. This is consistent with the behavior of a rocking wall where gap opening due to rocking forms at the base with the elastic wall deformations causing the drifts to increase with height (Acikgoz and DeJong 2012). Peak interstory drift and acceleration distributions along the height of the building are presented in Fig. 15 for representative ground motions at a low hazard level (43-year RP) and high hazard level (MCE_R) tests, indicating similar behavior.

Base Shear and PT Forces

Based on estimated seismic mass by floor (Table 3) and floor acceleration, the dynamic base shear was calculated for each test from the inertial forces summed over the 10 stories. Representative hysteresis plots from three different hazard levels are shown in Fig. 16. The estimated base shear through the entire test program reached a maximum of 770 kN (173 kips) during MID 88 in the X direction and 698 kN (157 kips) in test MID 88 in the Y direction. These maximum base shear values corresponded to 28% (X) and 26% (Y) of the total building weight. Recall that, for preliminary design, the base shear was calculated using the equivalent lateral force procedure in ASCE 7-16 assuming $R = 6$. This simplified procedure led to base shear demand equivalent to 8.3% of the weight [i.e., 226 kN (51 kips)], which is smaller than the actual base shear estimated from the acceleration data. The difference is at least partially attributable to the participation of higher modes, as described in the following, as well as the fact that the maximum base shear observed was associated with MCE_R level events.

The distributions of maximum base shear and PT forces from all tests are illustrated in Fig. 17. The PT force during testing did not vary by more than 16% [35.6 kN (8 kips)] from the initial PT force [222 kN (50 kips)]. Even though substantial wall uplift occurred during the tests, that uplift did not result in significant strain in the PT bars owing to their 34.1 m (113 ft) length. Therefore, the PT bars remained well below yield for all tests.

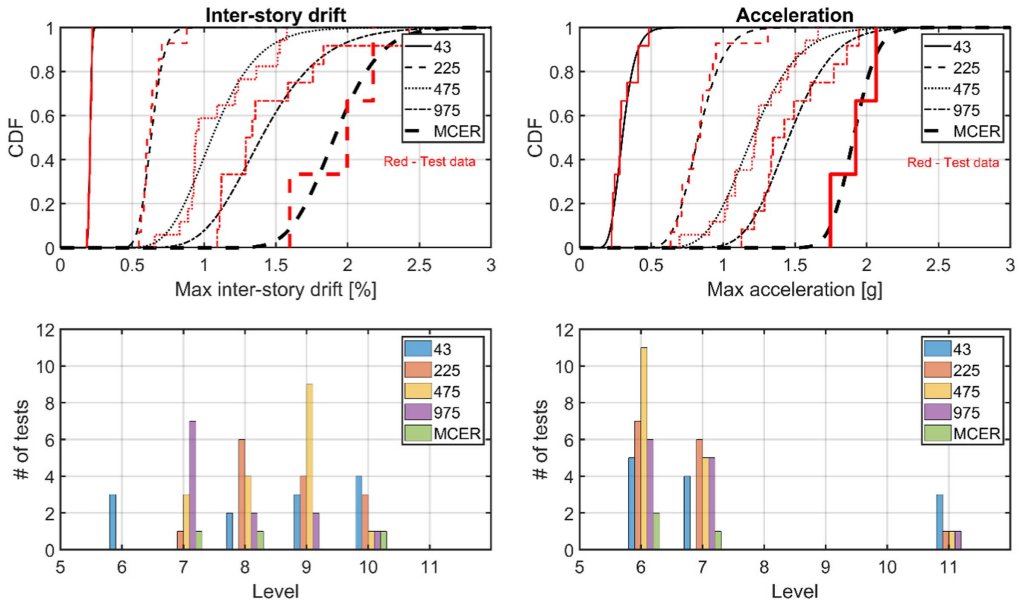

Fig. 14. CDF plots of maximum interstory drift and acceleration for each hazard level (bar chart indicates at which level the maximum drift or acceleration values were observed).

This work is made available under the terms of the Creative Commons Attribution 4.0 International license.

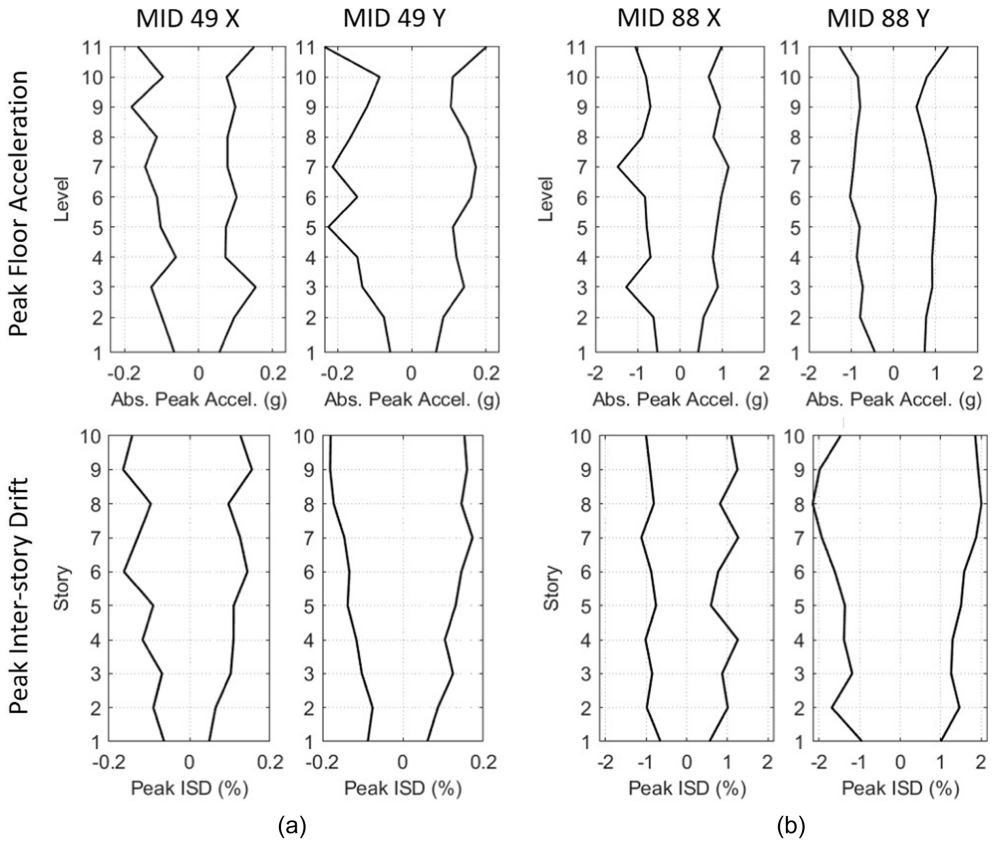

Fig. 15. Distribution of peak acceleration and interstory drift along the height of the building for: (a) representative 43-year RP ground motion; and (b) MCE_R ground motion.

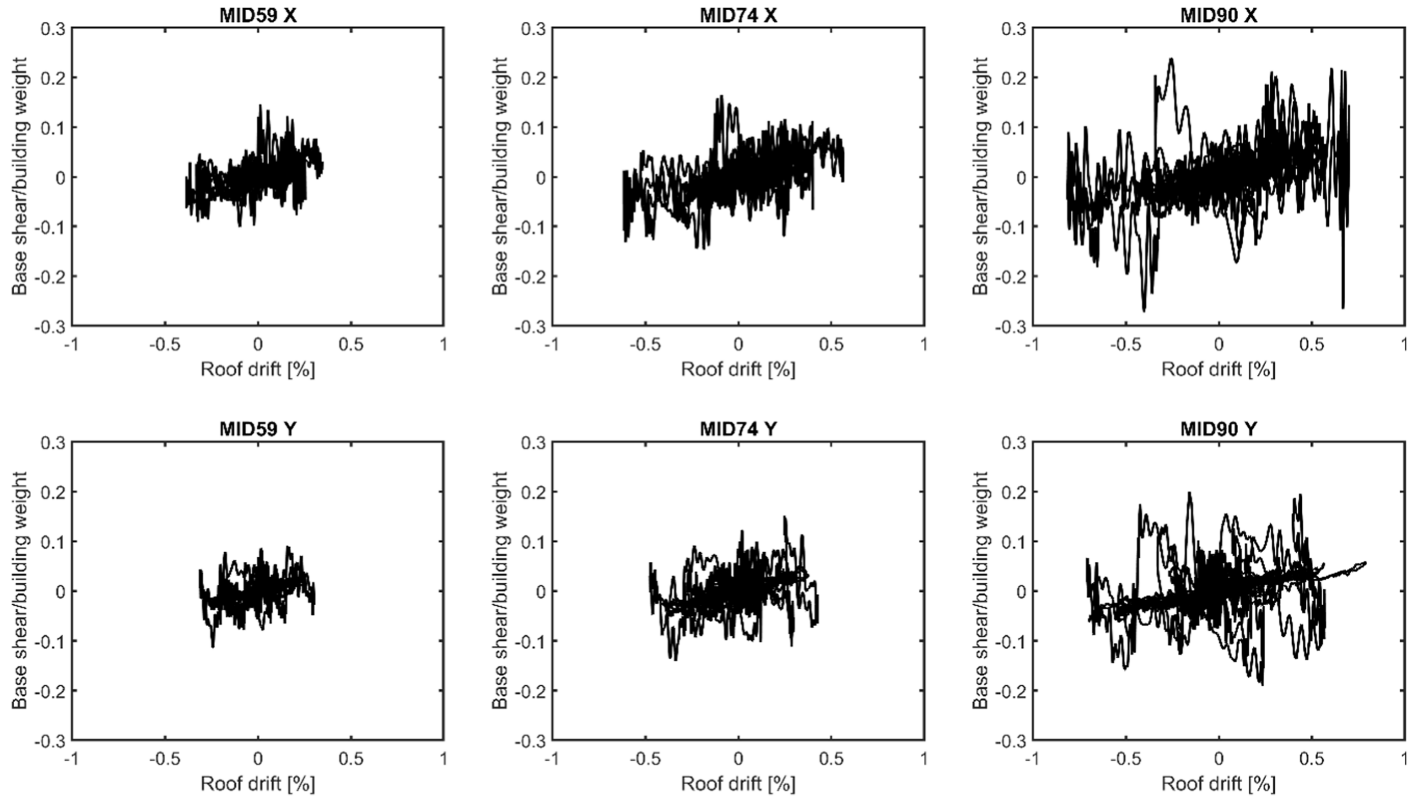

Fig. 16. Sample building global hysteresis responses at different hazard levels.

This work is made available under the terms of the Creative Commons Attribution 4.0 International license.

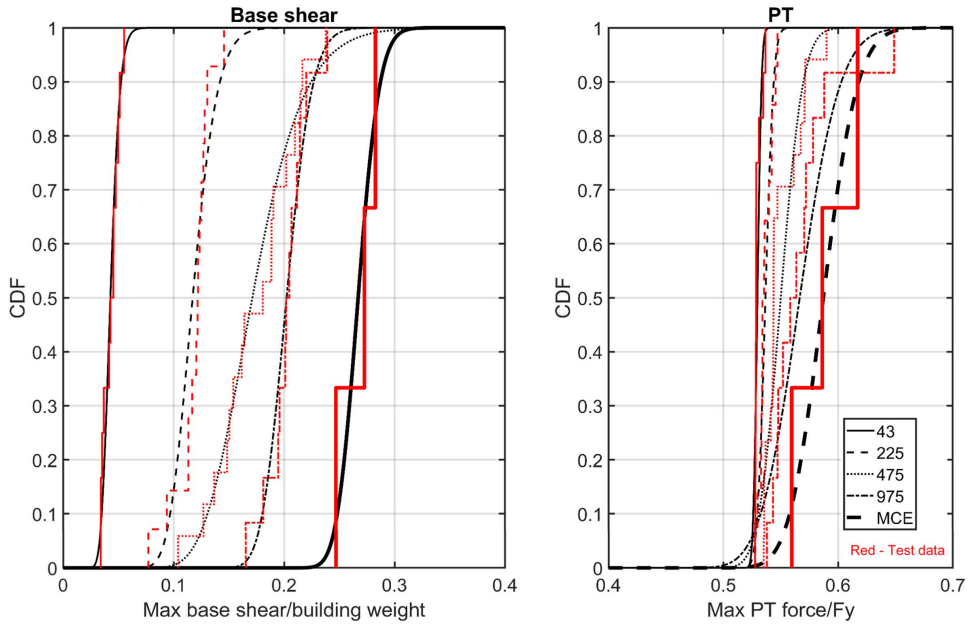

Fig. 17. CDF plots of maximum base shear and PT forces for each hazard level.

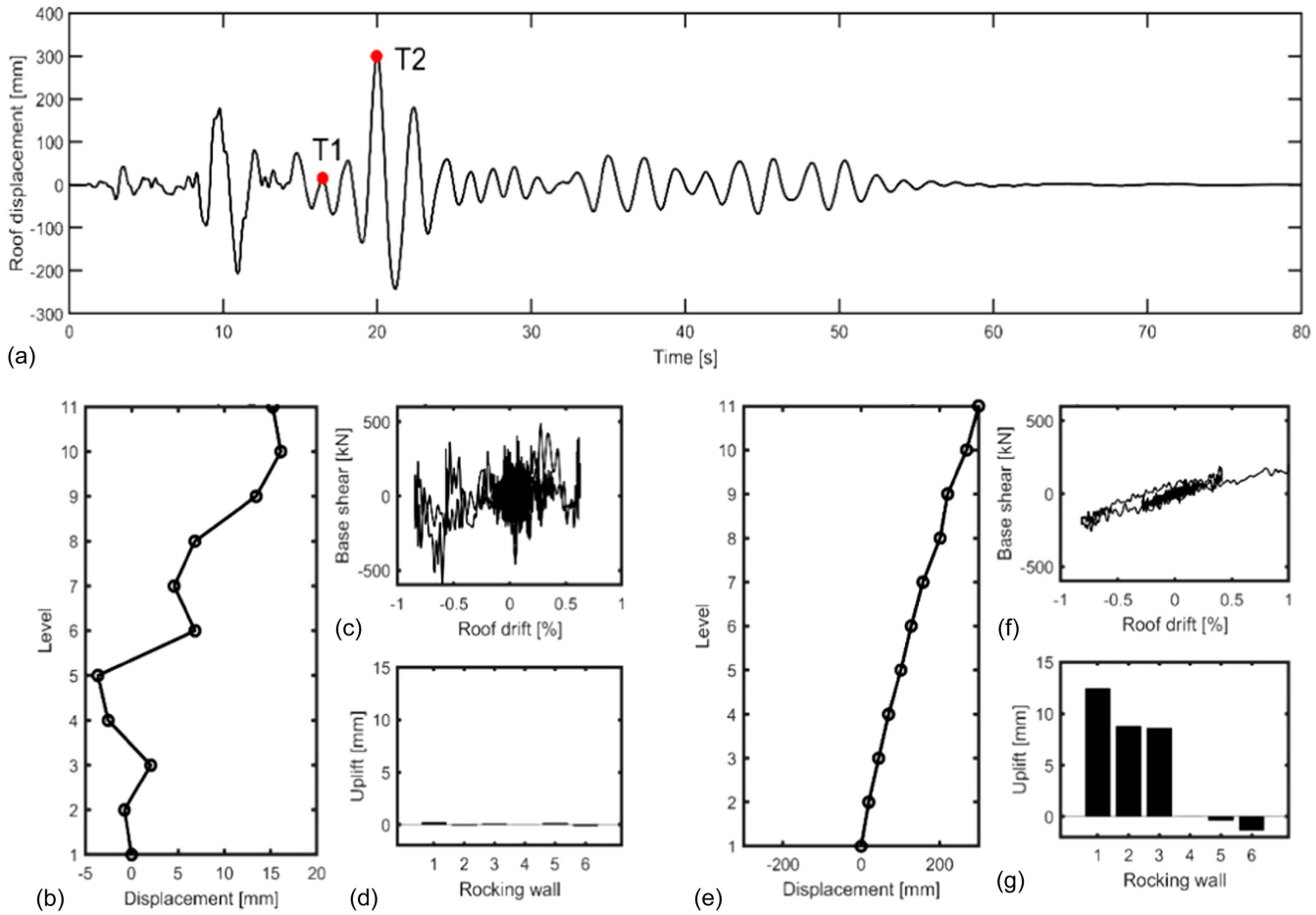

Fig. 18. Example response comparison between higher mode and first mode for MID 80: (a) roof time history in *X* direction; (b) floor displacement at T1; (c) global hysteresis from time 0 to T1; (d) base uplift profile at T1; (e) floor displacement at T2; (f) global hysteresis from time T2 to end; and (g) base uplift profile at T2.

This work is made available under the terms of the Creative Commons Attribution 4.0 International license.

Higher Mode Contributions

As briefly discussed, the response of the building included prominent higher-mode contributions that were visible to observers watching the tests. Data collected also reveal this distinct higher-mode participation. For example, the "spikes" observed in Fig. 16 in the hysteresis loops are likely a result of the higher-mode-induced accelerations. For example, responses from a 475-year RP test shown in Fig. 18 (Test MID80) illustrate substantial variation in the deformed shape of the building at different time points during the test (e.g., T1 vs. T2). There were clear higher-mode contributions to the deformed shape of the building at T1 [Fig. 18(b)], while the entire structure was dominated by the first mode response at T2 [Fig. 18(e)]. The global hysteresis from time 0 to T1 reveals many spikes in acceleration-induced base shear, indicating high force demands related to higher-mode effects [Fig. 18(c)]. However, the hysteresis from T2 to the end of the test is much smoother [Fig. 18(f)], which indicates more first mode dominated response correlated with larger rocking deformation (base uplift) measurements. As shown, the amount of wall base uplift (measured by six LVDTs along the base of the North CLT wall) was essentially zero at T1 [Fig. 18(d)] when the response was dominated by higher modes (sensors 1–3 are attached at the rocking toe at 0, 305, and 610 mm from the end of the wall; sensors 6, 5, and 4 were placed in the mirrored positions on the other end of the wall). At T2, the uplift was significant [Fig. 18(g)]. While large force demands and accelerations were observed during higher-mode responses, the maximum wall uplift, story drift, roof displacement, and PT force typically occur when the building is dominated by first mode response, which often happens toward the end of the earthquake excitations. It is also clear from the displacement time history that the building returned to its initial position without residual displacement.

Wall Out-of-Plane Brace Forces

For tall mass timber rocking walls, it is important in design and construction to ensure the wall panel is braced adequately in the out-of-plane direction. Because three of the rocking walls in the test structure are located at the edge of the diaphragm and the other is adjacent to the stair opening, the panels are only accessible for bracing on one side. Special braces were designed to transfer tension and compression forces from the rocking walls to the diaphragm [Fig. 7(e)]. The maximum bracing forces were calculated from strain gages installed on the braces (assuming uniform stress/strain through the section) and are presented in Fig. 19. During the design process, the out-of-plane bracing demand was calculated using the lateral bracing requirements for beams in AISC 360-16 (AISC 2016) as 55 kN (12 kips). As shown in Fig. 19, the measured demands increase with increasing seismic intensity but are all smaller than the estimated demand in design.

Gravity Frame and Diaphragms

The relative rotation of beam-to-column joints at selected locations were monitored using linear potentiometers during the test program. As described, a special beam-to-column connection was implemented in all gravity frame connections, allowing up to 0.05 rad rotation without damage. The maximum rotation measured from all tests at the selected joint locations was 0.025 rad. This is comparable with the maximum interstory drift estimated from corresponding floor acceleration measurements. While there were not enough sensors to monitor all gravity frame joints, damage inspection after each test revealed no visible damage or deformation on any joint, indicating that the performance of these connections was as expected.

The lateral demands for the design of the floor diaphragms were obtained from nonlinear response history analysis with the intention of keeping them damage-free even during the MCE_R level ground motions. Given the small footprint of the test building, the diaphragms acted rigidly and remained elastic during all testing. From damage inspections, there was no detectible deformation or damage to the floor systems through the entirety of the test program. For all tests, the lateral forces were effectively transferred to the rocking walls through the shear key detail shown in Fig. 7 with no damage or deterioration detected.

Impact of Ground Motion Directionality

Since the test program included a series of uniaxial, biaxial, and triaxial tests of the same ground motion record, data obtained from

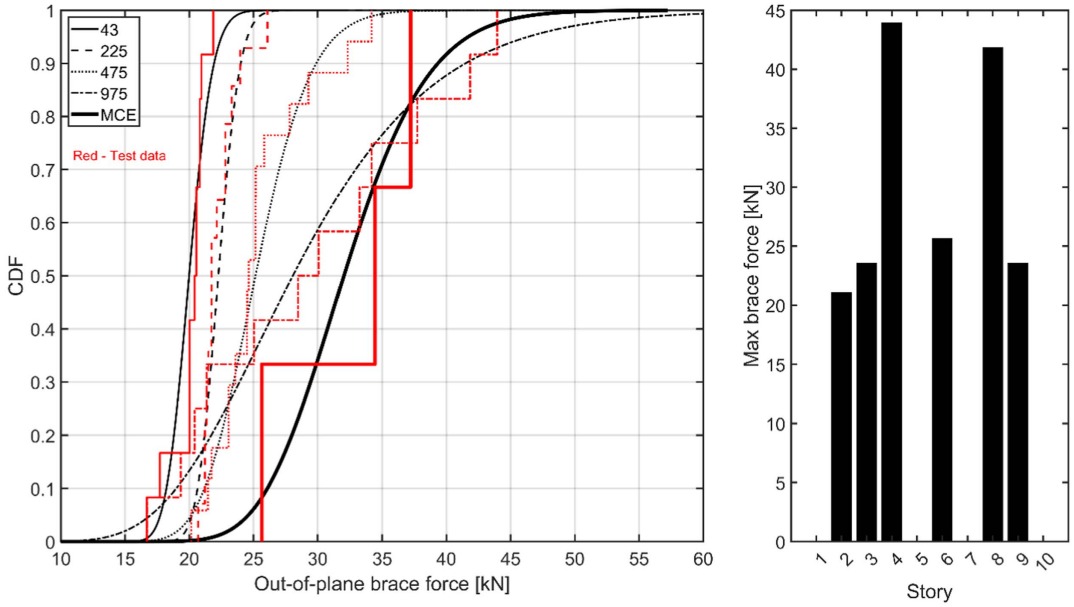

Fig. 19. Measured maximum rocking wall out of plane bracing demand and its distribution along building height.

This work is made available under the terms of the Creative Commons Attribution 4.0 International license.

these tests can aid in characterizing the impact of multiaxial excitation on the building's response. Because the original design expected some damage at the MCE_R level, the ground motions at the MCE_R intensity were applied directly as triaxial excitation when such input was within the capacity of the shake table. The rationale behind this decision is that, if damage were to occur, the opportunity to experience and observe that in 3D would be most valuable rather than "pre-damaging" the building in uniaxial or biaxial MCE_R tests. Thus, the comparison on directionality is only available for hazard levels up to the 975-year return period.

Fig. 20 shows representative roof displacement comparisons among uniaxial, biaxial, and triaxial tests using the same ground motion records at different intensity levels. Multiaxial loading had an insignificant effect on roof displacement up to the 975-year return period hazard. Fig. 21 summarizes the maximum values of key measurements from different excitation types and similarly shows that peak response quantities in one building direction were not significantly impacted by the addition of orthogonal and vertical ground motions. While the results are limited to the tested building with small torsional response, the fact that vertical ground motions did not affect the lateral response is a significant observation.

Nonstructural Systems Overview

In the following sections, a summary of nonstructural systems and components included in the test building is presented, along with key observations of their responses during testing. Drift compatible details were used in many of the components with drift capacity targeted at 2.5%. All nonstructural component connections were designed according to the anchorage force requirements in ASCE 7-16 Chapter 13, using MCE level seismic demands and setting $Rp/Ip = 1$ for elastic response. Minor to moderate damage to the nonstructural walls and stair components were observed at limited locations for intensities above 475-year RP hazard levels.

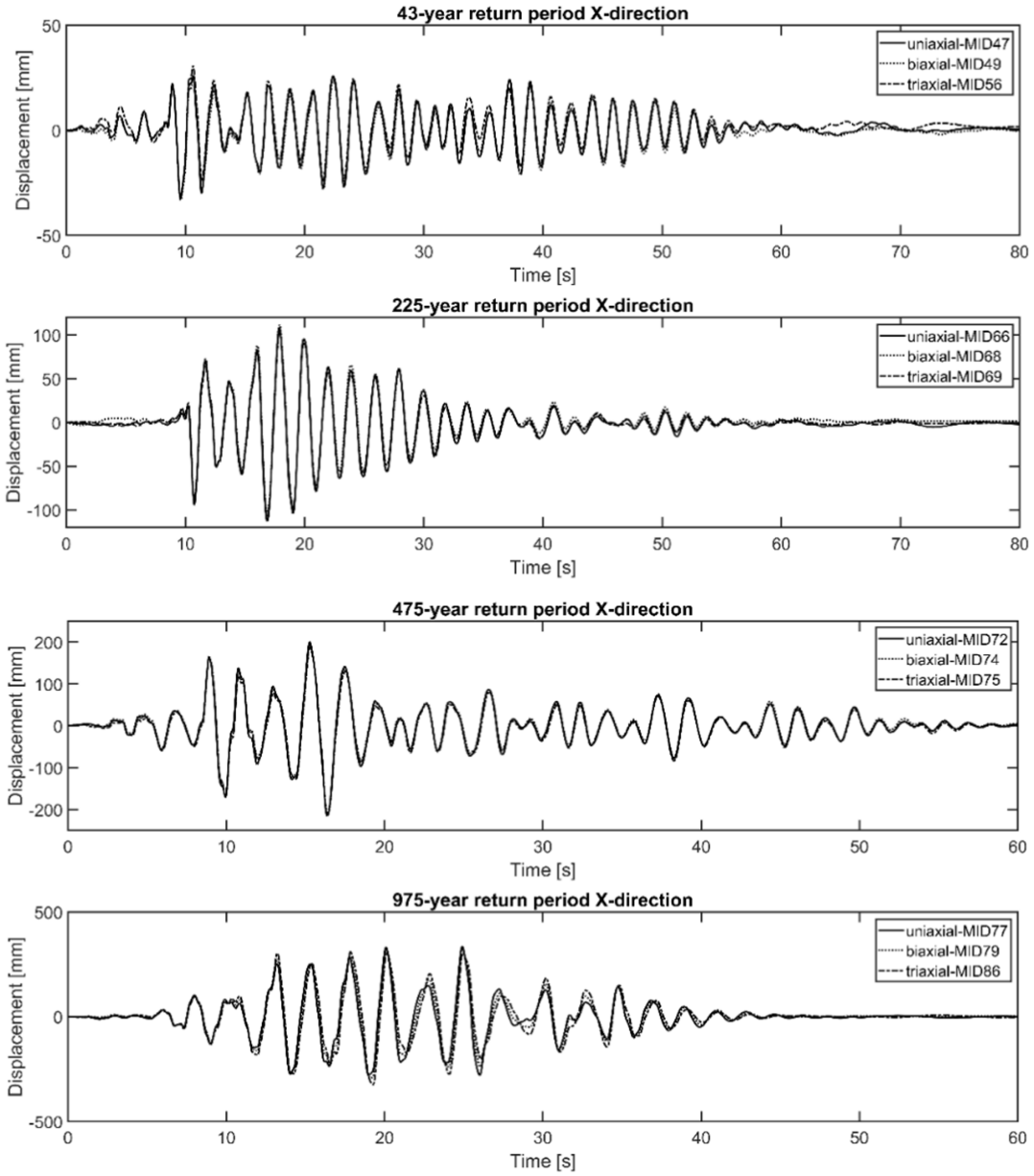

Fig. 20. Representative roof displacement time history comparison of multidirectional excitation conditions.

This work is made available under the terms of the Creative Commons Attribution 4.0 International license.

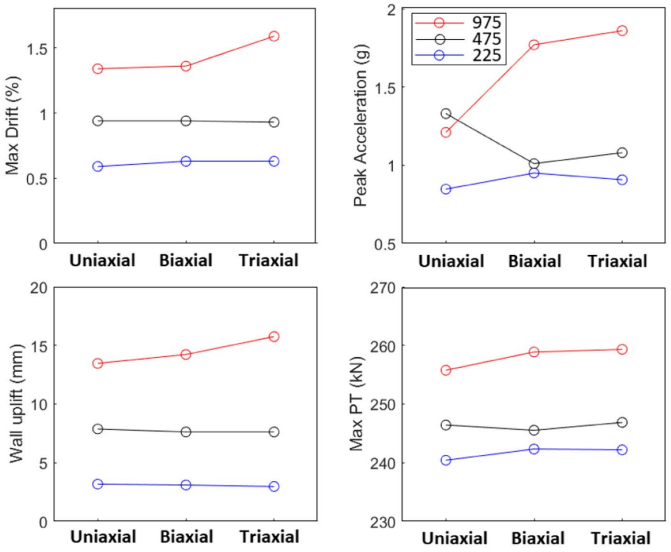

Fig. 21. Maximum response from ground motion with different directionality.

However, this damage would be mostly easy to repair (e.g., drywall repairs, reinforcement at some connections, possibly glass resetting) and would not affect the functionality of the building.

Exterior Façade Subassemblies

The building included four exterior façade subassemblies supported by the cantilevered concrete foundation blocks, one on each corner of the building (see Fig. 22). Three of the façades utilized cold-formed steel (CFS) framing, with drywall sheathing on the interior side, and fiberglass mat or steel-sheathed drywall sheathing on the exterior side with an aluminum composite panel skin finish outboard of a rainscreen drainage gap; and each were three stories tall. A variety of windows and one door were also included. The first L-shaped subassembly utilized platform framing, meaning the

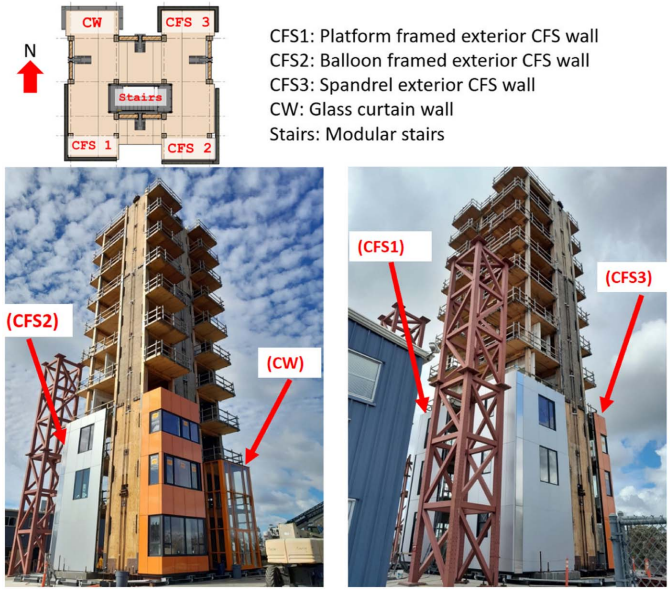

Fig. 22. Finished building with different exterior façade components. (Diagram adapted from Busch 2023; images by authors.)

walls are single-story units that bear directly on the floor slabs. Top-of-story slip track details and commercial expansion joints at wall intersections were incorporated to accommodate story drift. The second L-shaped subassembly utilized bypass framing, wherein the walls were constructed as multistory units hung or connected to the edge of the structural framing, in this case the floor slabs. To accommodate drift, a special drift clip was utilized that allows the attached wall to slide relative to the floor diaphragm, and a large expansion joint was incorporated at the intersecting walls to accommodate the accumulated drift incompatibility over three stories. The third C-shaped subassembly utilized alternating (stacked) layers of spandrel units and ribbon windows. This was also a bypass system in concept; however, the spandrel units were attached rigidly to the floor slabs, with interstory drift to be accommodated by a horizontal slip joint between the spandrels and the windows and displacement incompatibilities at corners to be accommodated directly by the window systems.

All three CFS-framed exterior walls performed well, and no major damage was observed throughout the test program. In the platform-framed subassembly, only the second story slipped significantly at the top of the wall as intended in design. The second story was the only one of the three that used a horizontally slotted track that allowed the slip mechanism to be between the top track and the diaphragm. In the third story, the lack of a corner joint to address the displacement incompatibility certainly limited slip. However, even without a joint, the corner detailing of the exterior panels proved to be robust enough to accommodate some movement through rotation of the panel along its connected axis. Slip may have been limited in the first story due to the presence of drywall screws across the double-track slip joint (a construction oversight issue). The bypass-framed system accommodated movement as expected, through sliding of the clips in the sliding track attached to the outside of the wall and opening/closing of the expansion joint cover at the corner. Some clips, mostly on the top level where the movement was largest, did not slide smoothly and tended to bind in the track, causing pullout of the screws attaching the clips into the studs, which was observed after the first few shakes at the 475-year RP. The clips were reinstalled or reinforced and monitored for the remainder of the test program. In the spandrel-framed system, minimal slip was observed across the slip joint; instead, the movement was accommodated almost entirely by the window systems, which was confirmed through video footage. The two different types of window systems utilized in the test program had very different mechanisms for accommodating the movement. The capacity of the windows to accommodate movement without any damage or glass cracking far exceeded what was expected. Further information about the CFS-framed facade subassemblies can be found in Roser et al. (2024).

The final exterior subassembly was a two-story, C-shaped glass curtain wall, a stick-built system with mechanically captured glass panels installed within horizontal and vertical mullions anchored to the floor slabs with vertically slotted anchors. This particular system was a specialty fire-rated curtain wall especially suited for the requirements of mass timber and incorporated 27 mm (1 1/16 in.) thick solid glass units and heavy-duty steel mullions. In contrast with the other systems, curtain walls absorb drift by racking of the framing and rotation of the glass within the frame. The curtain wall performed as expected and as intended; further, the movement of glass was visible from video footage and was significant. In addition, the typical racking and rotation of glass within the frame, vertical movement (bouncing) at the center of the glass panels was observed, which may have been a result of the vertical shaking that would not be present in typical quasistatic racking tests. One of the curtain wall panels on the west wall developed a permanent

This work is made available under the terms of the Creative Commons Attribution 4.0 International license.

displacement that increased over the progression of the shaking program such that eventually the edge of glass was exposed on the north side and disengaged from the gasket. No safety risk was posed as the glass was still fully captured on three sides. This mechanism was expected to breach air and water tightness but was also likely an artifact of the repeated shaking. Preliminary findings about the curtain wall are detailed in Wynn et al. (2024).

Interior Partition Walls

Interior walls were incorporated on stories four through six (see Fig. 23). The fifth- and sixth-story layouts originated from residential floor plans developed by an architect and then simplified to work within the limited building footprint. The fourth story utilized a conventional shaft wall around the stair core, while on the fifth story an alternative shaft wall concept was explored, which incorporated fire-rated panels surrounded by a flexible fire barrier into the stair framing. The interior partition walls featured interior doors in several locations, used double and slotted slip track details, and incorporated expansion joints wherever possible at wall corners to absorb differential movement between wall segments. In addition, two isolated wall subassemblies were installed on the sixth story to test a different type of expansion joint. The slip track details and varied expansion joints generally performed well to protect the partition walls. Thus, viable alternatives are available when the design context demands resilience. The biggest success was the design of an adjacent conventional interior to shaft wall connection that allowed for continuous slip across the interface. However, some damage to drywall was observed after the test, as shown in Fig. 23(d), even with the sliding track detail. This type of damage can be avoided by dropping the level of the gypsum board at the end of the wall. The preliminary observations of the interior partition walls response are detailed in Ji et al. (2024).

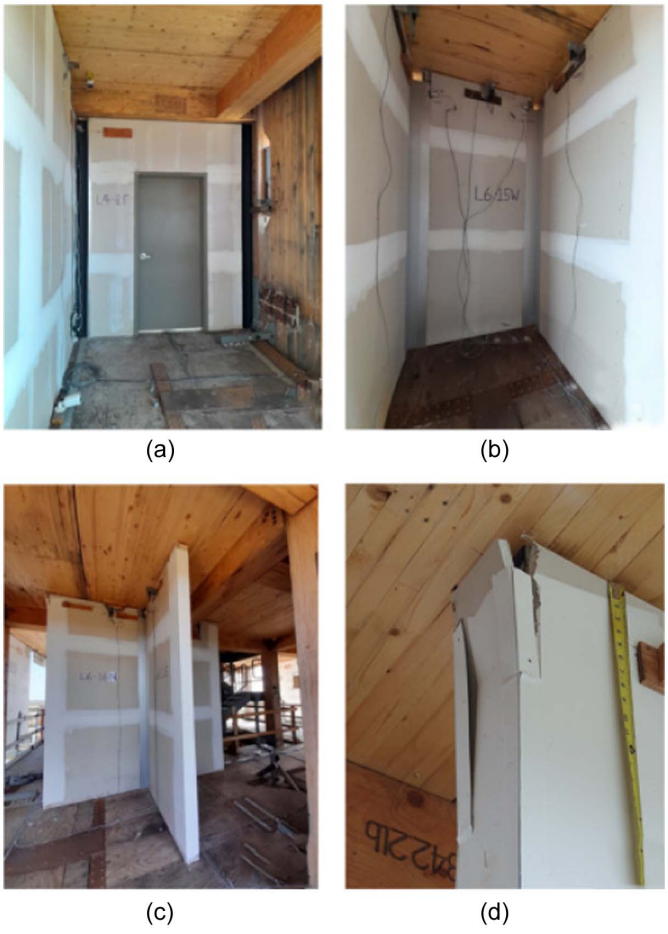

Fig. 23. Interior partition walls and typical damage: (a) interior wall with door; (b) C-shaped partition wall; (c) T-shaped partition walls; and (d) typical damage observed on partition walls. (Images by authors.)

Stair System

The stair tower was configured with its first eight stories utilizing a story-level complete modular unit (modular stair system [MSS]), and the remaining upper two stories (nine and ten) assembled with traditional (stick-framed) construction. The MSSs are self-supporting modules that were entirely preassembled in the shop and installed as a complete floor level within a building. Such a system is appealing, as it allows for shop-level control of construction tolerances and a reduction of on-site construction time. Traditional construction methods for stair systems, on the other hand, involve the assembly of individual subsystems (stair flights, handrails, landings, gravity columns) on-site and within a building during its construction.

The stair tower not only provided egress and ingress to the TallWood building but also an opportunity to investigate a range of connection methods, each designed to allow the stair system to effectively accommodate large interstory drift and thus serve as a resilient nonstructural system. In totality, two stories of the stair system were designed with fixed-free connections, two stories were designed with lateral and longitudinal slotted holes, and the remaining six stories were designed with a type of (previously tested and commercially available) drift-compatible connection (Fig. 24).

Throughout the test program, the stair system demonstrated robust, serviceable performance, suffering no loss of function during even the largest triaxial MCE_R motions. Although the stair system remained functional, minor damage was observed in the connections of many of the handrails, particularly during tests with larger-intensity (975-year and MCE_R). However, this damage did not render the stair system inoperable, though it indicates that there were stress points in the handrail connections that require attention or would benefit from refined design. The various types of connection detailing used in other key components of the stair system, notably the stair flights and treads, and gravity components such as landings and associated supports generally performed well. Preliminary analysis of measured response of the stairs indicates that peak floor accelerations were in line with diaphragm peak accelerations at the center of mass of the building. Even at the largest MCE_R motions, seismic force demands (as elicited from strain measurements) in the shear collector straps that transferred seismic shear from the stairs to the diaphragm were less than a third of yielding capacity. More detailed description and analysis on stair system performance can be found in Sorosh et al. (2024).

Conclusions

Based on the NHERI TallWood test results, it is concluded that tall wood buildings can achieve resilient seismic performance in regions of high seismicity. Posttensioned mass timber rocking walls coupled with a resilient mass timber gravity frame are practical and efficient to build and can provide structurally damage-free performance under repetitive seismic excitations at design and MCE_R hazard levels. Moreover, the incorporation of specially detailed nonstructural components within the test building provided excellent performance in triaxial earthquake excitations. In addition, the

This work is made available under the terms of the Creative Commons Attribution 4.0 International license.

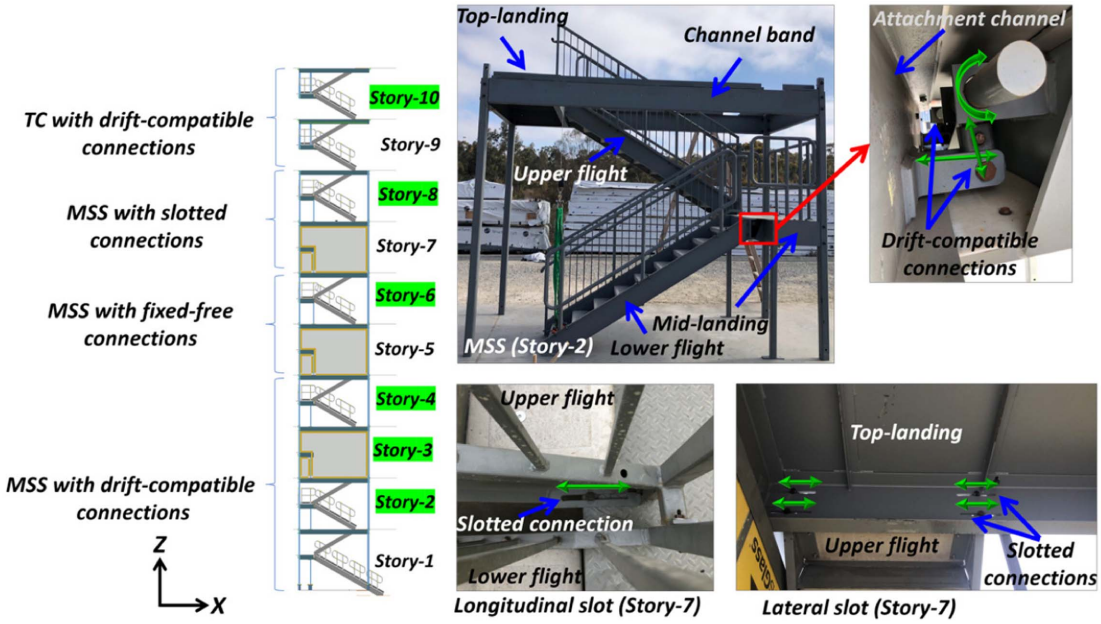

Fig. 24. Stair tower with instrumented stories highlighted in green, and a sample of stair connection details with degrees of freedom shown using green arrows. (Images by authors.)

data collected from the extensive test program will provide a landmark data set and effectively contribute to design and analysis of tall wood building response under earthquakes. The resilient performance of the tall wood building specimen will enhance confidence for the engineering community and the public for tall mass timber buildings for regions with high seismicity.

Specifically, the following key technical findings and conclusions can be summarized:

1. The test building had relatively long natural periods when compared with the approximated period formula used in ASCE/SEI 7-16 but aligned with the periods predicted by detailed numerical models. This observation is not unique to tall mass timber buildings (e.g., Tauberg et al. 2019). Rather, it is recognized in ASCE7 commentary that the approximate formula produces a lower-bound estimate of the period for a building of a given height.
2. Higher-mode effects caused high force demands but did not amplify deformation demands. The design method, which included the use of nonlinear response history analysis, used in this study addressed higher-mode forces adequately for this building.
3. No damage to the structural system was detected during physical inspections over the test program of 88 earthquakes. The resulting maximum drifts were relatively close to the design expectations. There was no residual drift observed, even after MCER level tests. However, the building's natural periods did elongate moderately over the testing program, likely due to local deformation of the mass timber panels at the rocking interface (corner crushing) and softening/damage to nonstructural systems.
4. Posttensioned mass timber rocking wall lateral system performed resiliently as designed. PT rods remained elastic during the tests; no fracture occurred on UFP devices; the glued-in threaded rod connections designed as the splice between rocking wall segments was able to successfully transfer the larger flexural and shear demands in the walls without evidence of damage. Lateral bracing designed for the rocking wall system performed well, which indicates that bracing demands for posttensioned rocking mass timber shear walls may be calculated using the nodal bracing force for beams based on AISC 360-16 (AISC 2016).
5. For the test structure, the impact of multiaxial excitation interaction was not significant for the main structural engineer demand parameters, which justified the design of rocking walls in each direction separately.
6. The resilient designed nonstructural systems of the test structure, which included interior partition walls, a variety of exterior facades, and a full-height stair tower, remained safe and fully operational throughout the test program, despite some repairable damage from the extensive number and intensity to MCER-scaled hazard motions imposed. Thus, there were no safety concerns regarding the means of ingress/egress for this building. However, protecting nonstructural systems using the methods proposed here may impose significant architectural constraints.

Data Availability Statement

Some or all data that support the findings of this study are available from the corresponding author upon reasonable request.

Acknowledgments

The NHERI TallWood Project is a collaborative research project, supported under National Science Foundation (NSF) awards 1636164, 1634204, 1635363, 1635156, and 1634628, carried out through collaboration with the U.S. Forest Service (USFS) through the Wood Innovation Fund Program, Forest Product Laboratory, and a large number of industry and nonprofit partners (NHERI Tallwood, n.d.). Any opinion expressed in this material is that of the authors and does not necessarily represent the opinion of sponsors.

References

Acikgoz, S., and M. J. DeJong. 2012. "The interaction of elasticity and rocking in flexible structures allowed to uplift." *Earthq. Eng. Struct. Dyn.* 41 (15): 2177–2194. https://doi.org/10.1002/eqe.2181.

This work is made available under the terms of the Creative Commons Attribution 4.0 International license.

AISC. 2016. *Specification for structural steel buildings*. Chicago: AISC.
Akbas, T., R. Sause, J. M. Ricles, R. Ganey, J. Berman, S. Loftus, J. D. Dolan, S. Pei, J. W. van de Lindt, and H. E. Blomgren. 2017. "Analytical and experimental lateral-load response of self-centering posttensioned CLT walls." *J. Struct. Eng.* 143 (6): 04017019. https://doi.org/10.1061/(ASCE)ST.1943-541X.0001733.
Amer, A., R. Sause, and J. Ricles. 2024. "Experimental response and damage of SC-CLT shear walls under multidirectional cyclic lateral loading." *J. Struct. Eng.* 150 (2): 04023215. https://doi.org/10.1061/JSENDH.STENG-12576.
Amini, M. O., J. W. van de Lindt, D. Rammer, S. Pei, P. Line, and M. Popovski. 2018. "Systematic experimental investigation to support the development of seismic performance factors for cross laminated timber shear wall systems." *Eng. Struct.* 172 (Oct): 392–404. https://doi.org/10.1016/j.engstruct.2018.06.021.
ASCE. 2016. *Minimum design loads and associated criteria for buildings and other structures*. ASCE/SEI 7-16. Reston VA: ASCE.
ASCE. 2022. *Minimum design loads and associated criteria for buildings and other structures*. ASCE/SEI 7-22. Reston VA: ASCE.
ATC (Applied Technology Council). 2021. "ATC hazards by location online tool." Accessed February 19, 2021. https://hazards.atcouncil.org/.
AWC (American Wood Council). 2018. *National design specification (NDS) for wood construction*. Leesburg, VA: AWC.
AWC (American Wood Council). 2021. *Special design provisions for wind and seismic (SDPWS)*. ANSI/AWC 2021. Leesburg, VA: AWC.
Blomgren, H. E., S. Pei, Z. Jin, J. Powers, J. D. Dolan, J. W. van de Lindt, A. R. Barbosa, and D. Huang. 2019. "Full-scale shake table testing of cross-laminated timber rocking shear walls with replaceable components." *J. Struct. Eng.* 145 (10): 04019115. https://doi.org/10.1061/(ASCE)ST.1943-541X.0002388.
Brown, J. R., M. Li, A. Palermo, S. Pampanin, and F. Sarti. 2021. "Experimental testing of a low-damage post-tensioned C-shaped CLT core-wall." *J. Struct. Eng.* 147 (3): 04020357. https://doi.org/10.1061/(ASCE)ST.1943-541X.0002926.
Busch, A. 2023. "Design and construction of tall mass timber buildings with resilient post-tensioned mass timber rocking walls." Ph.D. thesis, Dept. of Civil and Environmental Engineering, Colorado School of Mines.
Busch, A., R. B. Zimmerman, S. Pei, E. McDonnell, P. Line, and D. Huang. 2022. "Prescriptive seismic design procedure for post-tensioned mass timber rocking walls." *J. Struct. Eng.* 148 (3): 04021289. https://doi.org/10.1061/(ASCE)ST.1943-541X.0003240.
Ceccotti, A., C. Sandhaas, M. Okabe, M. Yasumura, C. Minowa, and N. Kawai. 2013. "SOFIE project–3D shaking table test on a seven-story full-scale cross-laminated timber building." *Earthquake Eng. Struct. Dyn.* 42 (13): 2003–2021. https://doi.org/10.1002/eqe.2309.
Deierlein, G., H. Krawinkler, X. Ma, M. Eatherton, J. Hajjar, T. Takeuchi, K. Kasai, and M. Midorikawa. 2011. "Earthquake resilient steel braced frames with controlled rocking and energy dissipating fuses." *Steel Constr.* 4 (3): 171–175. https://doi.org/10.1002/stco.201110023.
Field, T., A. R. Barbosa, R. B. Zimmerman, S. Pryor, A. Sinha, and C. Higgins. 2023. "Experimental and analytical evaluation of the tension capacity of edgewise connected glued-in rods in mass ply panels." *Constr. Build. Mater.* 409 (Dec): 133853. https://doi.org/10.1016/j.conbuildmat.2023.133853.
Ganey, R., J. Berman, T. Akbas, S. Loftus, J. Daniel Dolan, R. Sause, J. Ricles, S. Pei, J. V. D. Lindt, and H. E. Blomgren. 2017. "Experimental investigation of self-centering cross-laminated timber walls." *J. Struct. Eng.* 143 (10): 04017135. https://doi.org/10.1061/(ASCE)ST.1943-541X.0001877.
Gokhman, T. 2021. "Ascending timber aspiration in Milwaukee." *CTBUH J.* 1: 50–52.
Granello, G., A. Palermo, S. Pampanin, S. Pei, and J. Van De Lindt. 2020. "Pres-lam buildings: State-of-the-art." *J. Struct. Eng.* 146 (6): 04020085. https://doi.org/10.1061/(ASCE)ST.1943-541X.0002603.
ICC (International Code Council). 2021. *International building code*. Washington, DC: ICC.
Iqbal, A., M. Fragiacomo, S. Pampanin, and A. Buchanan. 2018. "Seismic resilience of plywood-coupled LVL wall panels." *Eng. Struct.* 167 (Jul): 750–759. https://doi.org/10.1016/j.engstruct.2017.09.053.
Iqbal, A., S. Pampanin, and A. H. Buchanan. 2016. "Seismic performance of full-scale post-tensioned timber beam-column connections." *J. Earthquake Eng.* 20 (3): 383–405. https://doi.org/10.1080/13632469.2015.1070386.
Iqbal, A., T. Smith, S. Pampanin, M. Fragiacomo, A. Palermo, and A. Buchanan. 2015. "Experimental performance and structural analysis of plywood-coupled LVL walls." *J. Struct. Eng.* 142 (2): 04015123. https://doi.org/10.1061/(ASCE)ST.1943-541X.0001383.
Ji, Y., K. L. Ryan, W. Roser, S. L. Wynn, T. C. Hutchinson, and R. Belvin. 2024. "Seismic response of non-structural cold-formed steel framed interior wall subassemblies with expansion joints." In *Proc., 18th World Conf. on Earthquake Engineering*. Tokyo: International Association of Earthquake Engineering.
Kordziel, S., S. Pei, S. V. Glass, S. Zelinka, and P. C. Tabares-Velasco. 2019. "Structure moisture monitoring of an 8-story mass timber building in the Pacific Northwest." *J. Archit. Eng.* 25 (4): 04019019. https://doi.org/10.1061/(ASCE)AE.1943-5568.0000367.
Kurama, Y., R. Sause, S. Pessiki, and L.-W. Lu. 1999. "Lateral load behavior and seismic design of unbonded post-tensioned precast concrete walls." *Struct. J.* 96 (4): 622–632.
LTBSDC (Los Angeles Tall Buildings Structural Design Council). 2023. *An alternative procedure for seismic analysis and design of tall buildings*. Los Angeles: LTBSDC.
Mazzoni, S., F. McKenna, M. H. Scott, and G. L. Fenves. 2006. *OpenSees command language manual*. Berkeley, CA: Pacific Earthquake Engineering Research Center.
NHERI Tallwood. n.d. "Industry leaders and collaborating researchers in tall wood." *Colorado School of Mines.* Accessed September 26, 2024. http://nheritallwood.mines.edu/collaboration.html.
Palermo, A., S. Pampanin, A. Buchanan, and M. Newcombe. 2005. "Seismic design of multi-story buildings using laminated veneer lumber (LVL)." In *Proc., New Zealand Society for Earthquake Engineering Conf.* Wairakei, New Zealand: New Zealand Society for Earthquake Engineering.
Palermo, A., F. Sarti, A. Baird, D. Bonardi, D. Dekker, and S. Chung. 2012. "From theory to practice: Design, analysis and construction of dissipative timber rocking post-tensioning wall system for Carterton Events Centre, New Zealand." In *Proc., 15th World Conf. on Earthquake Engineering*, 24–28. Tokyo: International Association of Earthquake Engineering.
Pei, S., J. W. van de Lindt, A. R. Barbosa, J. W. Berman, E. McDonnel, J. D. Dolan, H. E. Blomgren, R. B. Zimmerman, D. Huang, and S. Wichman. 2019. "Experimental seismic response of a resilient 2-story mass-timber with post-tensioned rocking walls." *J. Struct. Eng.* 145 (11): 04019120. https://doi.org/10.1061/(ASCE)ST.1943-541X.0002382.
Popovski, M., and I. Gavric. 2016. "Performance of a 2-story CLT house subjected to lateral loads." *J. Struct. Eng.* 142 (4): E4015006. https://doi.org/10.1061/(ASCE)ST.1943-541X.0001315.
Priestley, N. M. J. 1991. "Overview of the PRESSS research program." *PCI J.* 36 (4): 50–57. https://doi.org/10.15554/pcij.07011991.50.57.
Pryor, S., S. Pei, J. W. van de Lindt, and D. Huang. 2024. "Seismically resilient connections for mass timber buildings." In *Proc., World Conf. on Earthquake Engineering*. Tokyo: International Association of Earthquake Engineering.
Roser, W., K. L. Ryan, Y. Ji, S. L. Wynn, T. C. Hutchinson, C. Melcher, and R. Belvin. 2024. "Shake table test of a balloon-framed, cold-formed steel façade with drift clips." In *Proc., 18th World Conf. on Earthquake Engineering*. Tokyo: International Association of Earthquake Engineering.
Sarti, F., A. Palermo, and S. Pampanin. 2015. "Quasi-static cyclic testing of two-thirds scale unbonded posttensioned rocking dissipative timber walls." *J. Struct. Eng.* 142 (4): E4015005. https://doi.org/10.1061/(ASCE)ST.1943-541X.0001291.
Sarti, F., A. Palermo, S. Pampanin, and J. W. Berman. 2017. "Determination of the seismic performance factors for post-tensioned rocking

This work is made available under the terms of the Creative Commons Attribution 4.0 International license.

timber wall systems." *Earthquake Eng. Struct. Dyn.* 46 (2): 181–200. https://doi.org/10.1002/eqe.2784.

Sato, M., H. Isoda, Y. Araki, T. Nakagawa, N. Kawai, and T. Miyake. 2019. "A seismic behavior and numerical model of narrow paneled cross-laminated timber building." *Eng. Struct.* 179 (Jan): 9–22. https://doi.org/10.1016/j.engstruct.2018.09.054.

Skinner, R. I., J. M. Kelly, and A. J. Heine. 1974. "Hysteretic dampers for earthquake-resistant structures." *Earthq. Eng. Struct. Dyn.* 3 (3): 287–296. https://doi.org/10.1002/eqe.4290030307.

Smith, T., F. C. Ponzo, A. Di Cesare, S. Pampanin, D. Carradine, A. H. Buchanan, and D. Nigro. 2014. "Post-tensioned glulam beam column joints with advanced damping systems: Testing and numerical analysis." *J. Earthquake Eng.* 18 (1): 147–167. https://doi.org/10.1080/13632469.2013.835291.

Sorosh, S., T. C. Hutchinson, K. L. Ryan, K. Smith, R. Belvin, A. Kovac, S. Pei, and D. M. Dowden. 2024. "Performance of a 10-story steel stair tower within the NHERI Tallwood building." In *Proc., 18th World Conf. on Earthquake Engineering*. Tokyo: International Association of Earthquake Engineering.

Tauberg, N., K. Kolozvari, and J. Wallace. 2019. *Ductile reinforced concrete coupled walls: FEMA P695 study.* UCLA SEERL 2019/01. Los Angeles: UCLA Structural/Earthquake Engineering Research Laboratory, Univ. of California, Los Angeles.

USGS. 2017a. "NSHM: Conterminous U.S. 2014." GitHub Repository. Accessed September 27, 2024. http://github.com/usgs/nshm-cous-2014.

USGS. 2017b. "National seismic hazard mapping project (NSHMP) code." GitHub Repository. Accessed September 27, 2024. http://github.com/usgs/nshmp-haz.

van de Lindt, J. W., M. O. Amini, D. Rammer, S. Pei, P. Line, and M. Popovski. 2020. "Seismic performance factors for cross laminated timber shear wall systems in the united states." *J. Struct. Eng.* 146 (9): 04020172. https://doi.org/10.1061/(ASCE)ST.1943-541X.0002718.

van de Lindt, J. W., J. Furley, M. O. Amini, S. Pei, G. Tamagnone, A. R. Barbosa, D. Rammer, P. Line, M. Fragiacomo, and M. Popovski. 2019. "Experimental seismic behavior of a two-story CLT platform building." *Eng. Struct.* 183 (Mar): 408–422. https://doi.org/10.1016/j.engstruct.2018.12.079.

Van Den Einde, L., et al. 2021. "NHERI@ UC San Diego 6-DOF large high-performance outdoor shake table facility." *Front. Built Environ.* 6 (Jan): 580333. https://doi.org/10.3389/fbuil.2020.580333.

Wanninger, F., and A. Frangi. 2016. "Experimental and analytical analysis of a post-tensioned timber frame under horizontal loads." *Eng. Struct.* 113 (Apr): 16–25. https://doi.org/10.1016/j.engstruct.2016.01.029.

Wichman, S. 2023. "Seismic behavior of tall rocking mass timber walls." Ph.D. thesis, Dept. of Civil and Environmental Engineering, Univ. of Washington.

Wichman, S., J. W. Berman, and S. Pei. 2022. "Experimental investigation and numerical modeling of rocking cross laminated timber walls on a flexible foundation." *Earthquake Eng. Struct. Dyn.* 51 (7): 1697–1717. https://doi.org/10.1002/eqe.3634.

Wiebe, L., and C. Christopoulos. 2015. "Performance-based seismic design of controlled rocking steel braced frames. I: Methodological framework and design of base rocking joint." *J. Struct. Eng.* 141 (9): 04014226. https://doi.org/10.1061/(ASCE)ST.1943-541X.0001202.

Wynn, S. L., K. L. Ryan, W. Roser, Y. Ji, T. C. Hutchinson, and R. Madeley. 2024. "Seismic performance of a stick-built curtain wall system in a full-scale building shake table test." In *Proc., 18th World Conf. on Earthquake Engineering*. Tokyo: International Association of Earthquake Engineering.

Zimmerman, R. B., H. Blomgren, J. McCutcheon, and A. Sinha. 2021. "Catalyst—A mass timber core wall building with high ductility hold-downs in a seismic region." In *Proc., World Conf. on Timber Engineering*. Red Hook, NY: Curran Associates.

Zimmerman, R. B., and E. McDonnell. 2018. "Framework—Innovation in re-centering mass timber wall buildings." In *Proc., 11th U.S. National Conf. on Earthquake Engineering*. Red Hook, NY: Curran Associates.

This work is made available under the terms of the Creative Commons Attribution 4.0 International license.